



HAL
open science

Analysis of the effect of the 2D projection on droplet shape parameters

Victor Chéron, Jorge César Brändle de Motta, Jean-Bernard Blaisot, Thibaut Ménard

► **To cite this version:**

Victor Chéron, Jorge César Brändle de Motta, Jean-Bernard Blaisot, Thibaut Ménard. Analysis of the effect of the 2D projection on droplet shape parameters. *Atomization and Sprays*, 2022, 32 (8), pp.59-98. 10.1615/AtomizSpr.2022040525 . hal-03691512

HAL Id: hal-03691512

<https://hal.science/hal-03691512v1>

Submitted on 7 Mar 2023

HAL is a multi-disciplinary open access archive for the deposit and dissemination of scientific research documents, whether they are published or not. The documents may come from teaching and research institutions in France or abroad, or from public or private research centers.

L'archive ouverte pluridisciplinaire **HAL**, est destinée au dépôt et à la diffusion de documents scientifiques de niveau recherche, publiés ou non, émanant des établissements d'enseignement et de recherche français ou étrangers, des laboratoires publics ou privés.

Analysis of the effect of the 2D projection on droplet shape parameters.

V. Chéron[†], J.C. Brändle de Motta^{†,*}, J.B. Blaisot[†], T. Ménard[†]

[†] CORIA-UMR 6614 - Normandie Université, CNRS-Université et INSA de Rouen, Campus Universitaire du Madrillet,
76800 Saint Etienne du Rouvray, France.

* Corresponding author: jorge.brandle@coria.fr

September 3, 2021

1 **Abstract**

2 First, an analysis is done under the assumption of oblate or prolate spheroidal shape, which are representative
3 of droplets shape in a spray. Applying the assumption of random projection, the averaged value of the 2D
4 uniformity for a given 3D spheroid is computed. This analysis shows a wide dispersion of the 2D uniformity
5 values for the same spheroid. For prolate spheroids, the 2D uniformity systematically underestimates the
6 value of its 3D extension. When considering an oblate spheroid, the 3D value can be underestimated or
7 overestimated.

8 To assess this analytical analysis, two numerical droplets databases are considered: one based in homo-
9 geneous isotropic turbulence and one based on airblast atomization. Each database consists of 3D numerical
10 droplets with their 3D shape characterization, and, their projections in 2D. The results obtained analytically un-
11 der the assumption of spheroidal shape are confirmed on this database. In addition, the airblast database shows
12 clearly that the projection direction (i.e. the position of the camera) modifies the statistics on the morphology
13 of the drops.

14 As a conclusion, the results obtained from analytical and numerical experiments are extended to the exper-
15 imental results of atomization process where the 3D shape is unknown.

16 **Keywords: Shape parameters, Droplets characterization, Atomization**

17 **1 Introduction**

18 **1.1 Motivations**

19 Atomization of liquid is used in a variety of applications including combustion chambers, medical sprays, fire
20 suppression, and agricultural irrigation. Atomization is usually divided in two fragmentation steps: primary
21 atomization of the main liquid flow into detached liquid structures, and secondary atomization of these struc-
22 tures into spray droplets. Understanding these fragmentation processes is of tremendous interest and requires
23 the analysis and characterization of the different liquid elements encountered during these processes. Impor-
24 tant information is obtained by characterizing the shape of the liquid elements, to classify them into ligaments,
25 elongated or spherical droplets and then follow the space-time evolution of these characteristics in a given
26 atomization process.

27 Shadowgraphy or backlight imaging techniques are, among other methods, particularly good candidates
28 to carry out shape characterization analysis in spray applications [Bachalo and Houser, 1984, van Beeck and
29 Riethmuller, 1996, Schober et al., 2002, Bothell et al., 2020]. A projection on the image plane of the liquid
30 phase elements is obtained by these techniques. The liquid-gas interface is then obtained by analyzing the
31 contour of the liquid elements in this 2D projection along with different parameters such as the projected area,
32 the sphere-equivalent diameter. Several shape parameters are derived from this contour. It should be noted that
33 these parameters, while useful to characterize liquid structures in a spray, are obtained from 2D projections
34 and the shape of liquid elements is intrinsically three-dimensional. This 2D projection results in a loss of
35 information in experimental data.

36 It is often assumed that elongated liquid elements have a symmetry axis parallel to the image plane and
37 assumed spherical when the apparent shape is circular. However, these assumptions can be misleading, as
38 illustrated in the image sequence of a water jet emanating from a triple-disk nozzle in figure 1. This jet, ex-
39 tensively analyzed by our research group using different shape parameters [Dumouchel and Blaisot, 2014] and
40 multi-scale analysis [Dumouchel and Blaisot, 2013, Dumouchel et al., 2015], is characterized by a plane liquid
41 sheet that disintegrates asymmetrically in ligaments and droplets. First, the plane geometry of the liquid core,
42 see position I in the figure, is difficult to comprehend only from the image and without additional information.
43 Second, the droplet at position II has a near circular projection, suggesting a spherical shape. Nevertheless, the
44 sequence shows that the droplet follows oscillations after the break-up of the ancestor ligament and exhibit a

45 somewhat flat pancake-like shape as indicated at position III.

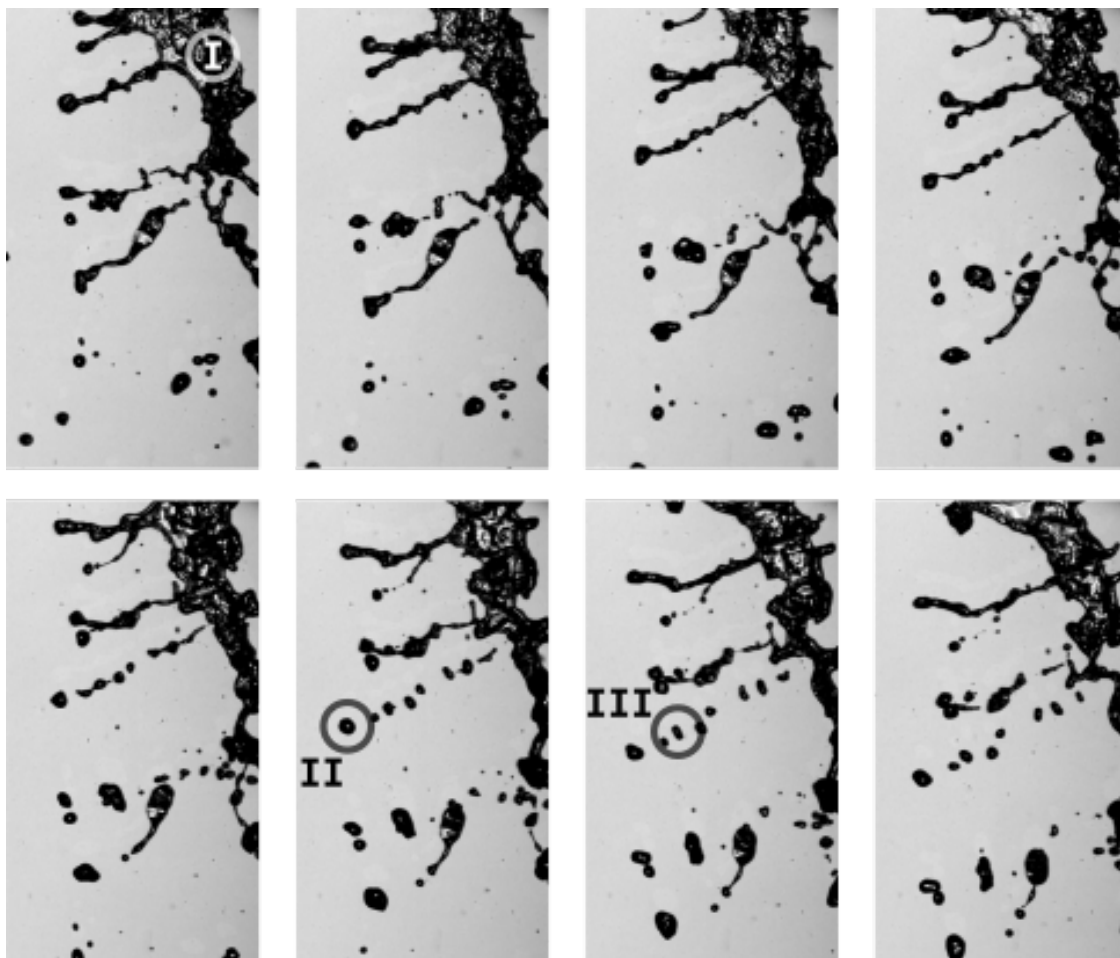


Figure 1: Shadowgraphy image sequence (25 000 frames/s) of a liquid jet [Dumouchel and Blaisot, 2014]. The field of view is $3.5 \text{ mm} \times 6.4 \text{ mm}$. Refer to text for roman letters.

46 These examples show the deviation due to the projection of a real 3D shape that can be introduced in the
47 analysis of 2D experimental images. To the authors' knowledge, few experiments have been performed to get
48 3D shape characteristics of liquid-gas interface elements in two-phase flows, and most of them are devoted to
49 bubble dynamics and breakup [Ravelet et al., 2011, Masuk et al., 2019]. The lack of 3D experimental data
50 in sprays is due to the challenging environment of the atomization processes: i.e. high velocity, large number
51 of droplets, optical access limitations, etc., along with the absence of diagnostic techniques that is capable of
52 capturing reliable 3D information in such conditions. The analysis of 3D shapes is more common in granular
53 and porous material communities where each structure can be extracted individually, such as in grain analysis
54 [Rorato et al., 2019]. A common way to compute the 3D shape parameters is by analyzing three orthogonal
55 projection of the structure [Blott and Pye, 2008].

56 The spray community call on CFD to get 3D information on atomizing flows [Dumouchel et al., 2015].

57 This is also what is done here to analyze the systematic error in shape analysis resulting from the 2D projection
58 in experiments. The paper combines an analytic study under the spheroid assumption, numerical simulations
59 for detailed analysis of realistic droplets, and, an application to experimental data.

60 Shape parameters under consideration for 2D and 3D analysis are detailed in §1.2. In §2, the CFD flow
61 solver and the detection algorithm are briefly described. At the end of this section, the droplet database ob-
62 tained from the CFD solver used is presented. Two test cases are considered for CFD, yielding to two typical
63 atomization conditions, i.e. (i) isotropic and (ii) anisotropic deformed droplets. In §3, the shape parameters
64 are analytically analyzed under the spheroid assumption and the limits of this assumption is commented using
65 the droplet database. In §4, the analysis of shape parameters is done on the droplet database, first for isotropic
66 droplets and next for anisotropic deformed droplets. The systematic deviation due to the projection step is
67 highlighted in this section, showing a correlation with the new method introduced in section §3 for analyzing
68 2D shape parameters based on the spheroid assumption. In §5, this new procedure is applied to a droplet
69 database obtained from an experimental setup. A correlation between the shape parameter probability density
70 function of the distributions and a log-normal distribution is shown, creating a possibility to reproduce a 3D
71 shape parameter distribution from 2D information under certain hypotheses.

72 **1.2 Summary of morphological parameters**

73 A liquid drop can take on an infinite number of distinct shapes. A significant number of shape parameters
74 have been created in the literature to account for this large variety of shapes. As pointed out by [Ghaemi et al.,
75 2009], the nomenclature diverges among authors. As a result, the definitions of the morphological or shape
76 criteria utilized must be clarified. These definitions are first detailed for 2D analysis, and then for 3D analysis.
77 The 2D case refers to the experimental works, mainly using image for shape analysis. In such cases, a kind
78 of projection is performed between the real 3D droplet and the 2D image object. The 3D case refers to CFD
79 data that can provide such information not reachable from the experiment. Even if the dimension of the shape
80 parameter space can be considered as infinite, practical morphology analyzes concentrate on a few parameters.
81 The four parameters under consideration in this study are resumed in table 1 with their mathematical definition
82 in 2D and 3D, and their ranges of variation. The shape parameter values are illustrated in figure 3 for two
83 objects.

84 1.2.1 2D parameters

85 Shape parameters are defined from the value of primary parameters measured on the contour of a droplet \mathcal{D}
86 such as the contour length (perimeter $p_{\mathcal{D}}$), the contour area ($A_{\mathcal{D}}$ and maximum and minimum lengths a_{2D} and
87 b_{2D} measured on two particular points on the contour (see below). Four shape parameters were selected in this
88 study for their relevance to the objectives of this work. The primary parameters used for the 2D definition of
89 these parameters are illustrated in figure 2 on an arbitrary shape droplet \mathcal{D} . As the final shape of any droplet in
90 a spray is a sphere, the 2D projected droplet is compared with a circle \mathcal{C} of the same projected surface area $A_{\mathcal{D}}$,
91 with its center coinciding with the droplet centroid. This circle is called the equivalent circle within this paper.
92 Thus the equivalent radius, $R_{EQ,2D}$, is defined as the radius of the equivalent circle, i.e. $R_{EQ,2D} = \sqrt{\frac{A_{\mathcal{D}}}{\pi}}$ (see
93 the horizontal dashed circle figure 2).

94 **Aspect ratio** $\alpha_{2D} = \frac{b_{2D}}{a_{2D}}$

95
96 The aspect ratio [Eriksson et al., 1997], also called centricity [Ghaemi et al., 2008], is the ratio between two
97 lengths, b_{2D} and a_{2D} , where $b_{2D} < a_{2D}$, i.e. $0 \leq \alpha_{2D} \leq 1$. Different computations of these lengths can be
98 found in the literature. It is for example expressed as the lengths of the smallest rectangle that contains the
99 object [Baert et al., 1992, Malot and Blaisot, 2000]. A similar implementation is the computation of a_{2D} as the
100 length of the segment between the two most distant points on the object contour and b_{2D} the maximum distance
101 between two points connected by a segment perpendicular to the first segment [Mayor et al., 2005, Kashdan
102 et al., 2007]. In these two configurations, a disc or a square have an aspect ratio of 1. Other authors consider
103 the extremes distances from the centroid of the object to the contour [Adrian, 1991, Adrian, 2005]. In such
104 a case the aspect ratio of a square is $\frac{\sqrt{2}}{2}$. This later definition is the one used in the present paper. It can be
105 noted that for the particular case of an ellipse, these distances are measured on two perpendicular lines and the
106 different definitions of a_{2D} and b_{2D} lead to the same value of the aspect ratio, α_{2D} .

107 **Uniformity** $\eta_{2D} = \frac{a_{2D} - b_{2D}}{R_{EQ,2D}}$

108
109 The uniformity parameter [Blaisot and Yon, 2005] is the difference $a_{2D} - b_{2D}$ normalized by $R_{EQ,2D}$. It is
110 a length-based parameter that can be useful to discriminate small surface ripples from elongated droplets. A
111 small value indicates small scale ripples compared to the object size whereas a large value is associated to
112 ligaments.

113

114 **Irregularity** $\iota_{2D} = \frac{p_C}{p_D}$

115

116 This parameter is defined as the ratio between the perimeter p_C of the equivalent circle \mathcal{C} and the contour
 117 perimeter p_D of the object [Podczeck et al., 1999]. As based on the total length of the object contour, this pa-
 118 rameter is more likely to capture small shape deformations. Naturally, this parameter is very sensitive to small
 119 scale deformation of the contour. This can be a drawback for practical application where the interface cannot
 120 be accurately obtained (e.g. false small-scale wrinkling due to pixelized interface contour) [Mayor et al., 2005].

121

122 **Symmetric difference shape parameter (SDS)** $\psi_{2D} = \frac{A_{\mathcal{D} \cup \mathcal{C}} - A_{\mathcal{D} \cap \mathcal{C}}}{A_D}$

123

124 The SDS parameter introduced by [Malot and Blaisot, 2000] is defined by the symmetric difference between
 125 \mathcal{D} and \mathcal{C} (dashed areas on the figure 2), normalized by the object area A_D . This parameter is null for a perfect
 126 disc and is bound by 2, a value reached when the object and the equivalent circle have no common part.

127 The definitions and the range of values for all these parameters are given in table 1. An illustration of the
 128 particular values taken by the parameters for three directions of projections of two typical shapes; a prolate
 129 spheroid and a tube, are given figure 3. It is recalled to the reader that a meticulous description of 2D shape pa-
 130 rameters and their application is provided in [Ghaemi et al., 2009]. The influence of the direction of projection
 131 is commented in the presentation of the 3D morphological parameters.

132 **1.2.2 3D parameters**

133 Whereas many definitions can be found in the literature about 2D shape parameters, to the authors knowledge,
 134 the existing 3D morphological parameters have not been studied in the past in the framework of atomization.
 135 This is mainly due to the fact that experimental techniques provide only 2D information. In the present study,
 136 the 2D parameters have been extended to the 3D domain reachable from CFD to obtain the 3D shape param-
 137 eters. The main quantities used to build 3D parameters are: the minimal and maximal distance from the 3D
 138 centroid to the 2D interface, b_{3D} and a_{3D} , respectively. The total surface and volume of the droplet, S_D and V_D
 139 respectively. These latter quantities are used as equivalence in 3D to the perimeter and projected area in 2D for
 140 the shape parameter definitions.

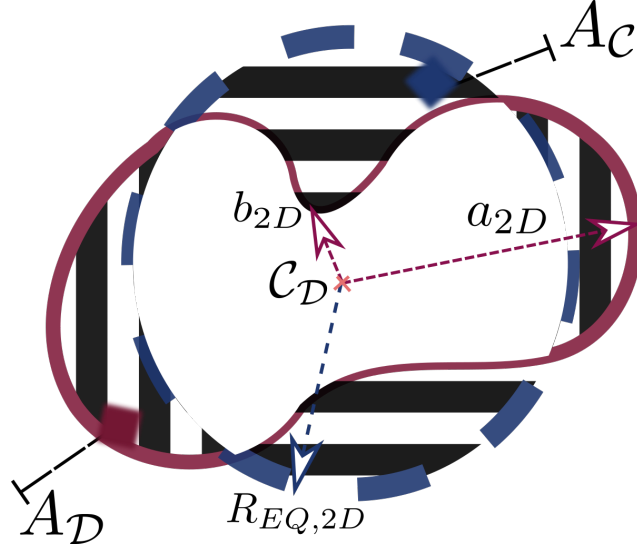


Figure 2: Definition of distances and shape parameters construction for the projection of a peanut-like droplet, vertical dash lines, and its equivalent circle, horizontal dash lines. The union of these two shapes, $A_{D \cup C}$ contains these two areas and the intersection of these two shapes, $A_{D \cap C}$, in filled white.

141 Aspect ratio and uniformity are constructed in their 3D extension with similar lengths (i.e. 1D information).
 142 The 3D equivalent radius is defined from the equivalent sphere that has the same volume than the volume
 143 of the droplet V_D , i.e. $R_{EQ,3D} = \sqrt[3]{\frac{3V_D}{4\pi}}$. The total surface of the equivalent sphere $S_S = 4\pi R_{EQ,3D}^2$, is
 144 used to compute the irregularity. Similarly to its 2D version, the accuracy of the irregularity depends on the
 145 resolution of the interface. Finally, the equivalent symmetric difference shape parameter (SDS parameter)
 146 [Malot and Blaisot, 2000] is defined from the common volume between the droplet and the equivalent sphere.
 147 This parameter is very sensitive to numerical accuracy since every cell has to be checked and compared to
 148 the equivalent sphere. In this paper, an additional step is used for each cell containing the interface of the
 149 equivalent sphere and the droplet. It consists in a subdiscretization of the Cartesian cell with 15 points per
 150 direction, improving the accuracy of the computation of the volume of intersection in each cell.

Parameter	2D Expression	3D Expression	Bounds	References
Aspect ratio	$\alpha_{2D} = \frac{b_{2D}}{a_{2D}}$	$\alpha_{3D} = \frac{b_{3D}}{a_{3D}}$	$[0, 1]$	[Eriksson et al., 1997]
Uniformity	$\eta_{2D} = \frac{a_{2D} - b_{2D}}{R_{EQ,2D}}$	$\eta_{3D} = \frac{a_{3D} - b_{3D}}{R_{EQ,3D}}$	$[0, \infty[$	[Blaisot and Yon, 2005]
Irregularity	$l_{2D} = \frac{p_C}{p_D}$	$l_{3D} = \frac{S_S}{S_D}$	$[0, 1]$	[Podczeczek et al., 1999]
SDS parameter	$\psi_{2D} = \frac{A_{D \cup C} - A_{D \cap C}}{A_D}$	$\psi_{3D} = \frac{V_{D \cup S} - V_{D \cap S}}{V_D}$	$[0, 2[$	[Malot and Blaisot, 2000]

Table 1: 2D and 3D morphological parameters analyzed throughout the present communication.

151 To illustrate the values that the shape parameter can take, two particular objects are considered, i.e. a
 152 prolate spheroid representative of a droplet and a tube representative of a ligament. The values taken by the 2D

153 and 3D parameters for these objects are shown in figure 3. It clearly shows the dependence of these parameters
 154 on the object shape. Indeed, the tube can be seen as an elongation of the prolate spheroid but its 3D parameter
 155 values are drastically different from those of the prolate spheroid. The figure shows also the sensitivity of the
 156 2D parameter values on the object orientation relative to the projection plane. It can easily be guessed from
 157 these examples that a small variation of the main axis orientation can strongly modify the values for all the 2D
 158 shape parameters, for the 3D tube as well as for the prolate spheroid.

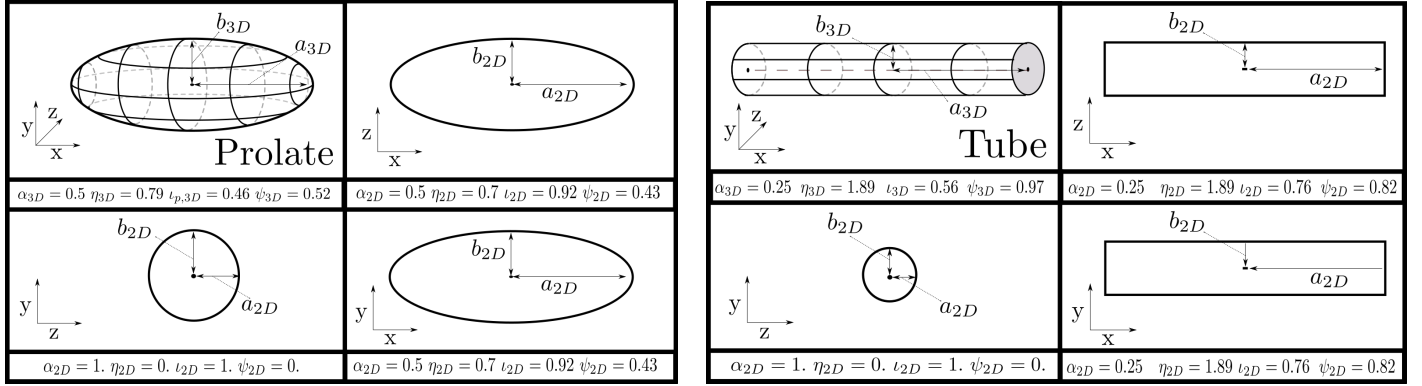


Figure 3: Projection of two specific 3D shapes: a prolate spheroid and a tube, respectively left and right. Morphological values for the 3D and each projection are given, respectively the aspect ratio; α , the uniformity; η , the irregularity; ι , and the SDS parameter; ψ .

159 2 Numerical procedure

160 Direct numerical simulation is an ideal tool to study the shape evolution of droplets. The projection of 3D
 161 simulated droplets generates experimental shadowgraphy-like images that can be analyzed to understand the
 162 deviation between 3D and 2D parameters. Two numerical experiments are treated in this paper. The present
 163 section introduces the CFD solver, the projection approach and the two configurations.

164 2.1 Flow solver

165 The in-house solver *Archer* has been used to perform the direct numerical simulations analyzed in the present
 166 communication. This solver has been developed during the last 15 years and has been successfully applied to
 167 the study of atomization process [Lebas et al., 2009], two-phase turbulence [Duret et al., 2012] and microfluidic
 168 [Charpentier et al., 2020].

169 This solver uses a projection algorithm to solve Navier-Stokes equations over a staggered Cartesian mesh.

170 The sharp interface is treated using a Coupled level set Volume-of-Fluid approach [Ménard et al., 2007]. Con-
171 vective terms are discretized using a fifth order WENO scheme to treat the interface discontinuities. The
172 viscous terms are discretized following the method proposed by [Sussman et al., 1998]. The Poisson equation
173 is solved using a conjugate gradient solver [Tanguy and Berlemont, 2005], and it includes the pressure drop
174 due to surface tension, that is discretized using the ghost fluid method [Fedkiw et al., 1999]. A momentum con-
175 servative approach is also implemented to ensure the consistency between the mass and momentum equations
176 in Navier-Stokes, [Vaudor et al., 2017].

177 The choice of *Archer* is done since its capabilities to simulate atomization under harsh environment and
178 ensuring an accurate description of the liquid-gas interface have been shown.

179 **2.2 Detection, projection and morphological parameter computation**

180 In *Archer*, a detection algorithm based on the developments of [Herrmann, 2010b] is used to extract each
181 individual droplet in 3D. This algorithm provides for each cell a tag corresponding to the droplet number. To
182 ensure that the shape analysis of the droplet does not consider other structures, each droplet is transported to a
183 numerical box, and, the liquid of any cell containing a different tag is removed. If necessary, the reinitialization
184 algorithm included in *Archer* is applied to ensure that the level set is accurately representing the interface. Then,
185 the 3D morphological parameters are computed in this domain, following the methodology given by [Chéron
186 et al., 2019, Chan et al., 2021].

187 Once each droplet is isolated, the projection is done to reproduce experimental results from shadowgraphy
188 analysis. The strategy is to consider each cell as a single pixel, and, to use the information from the projection
189 of the 3D field. In this case, the level set is used. A 16 bits gray value for each pixel is given, based on the
190 256^2 possible gray values. The pixel identified at the interface has the threshold value of $65536/2$. It can
191 be identified with the iso-value 0 of the level set field. These experimental-like images are sent to the same
192 algorithm used to analyze experimental images [Fdida et al., 2010]. Finally, 2D morphological parameters are
193 calculated for each direction of 2D projection (i.e. 3 per droplet).

194 **2.3 Droplet immersed in a Homogeneous Isotropic Turbulent-like flow**

195 The first numerical experiment consists in the study of a single droplet immersed in a Homogeneous Isotropic-
196 like Turbulence, (HIT-like). Interactions between turbulent flows and droplets are studied using such approach

197 by different authors [Trontin et al., 2010, Perlekar et al., 2012, Duret et al., 2012, Dodd and Ferrante, 2016].
198 The methodology is to use a tri-periodic domain to develop a turbulent flow with two immiscible phases. The
199 main difference in the present configuration is that only one droplet is considered. Thus, its evolution can be
200 studied without dealing with other phenomena such as breakup or coalescence. In addition, the high resolution
201 of the droplet can be guaranteed, and, thousands of droplets can be studied with low numerical cost. The main
202 drawback of this configuration is that the turbulence is not fully developed. Since the authors are not analyzing
203 here the turbulent properties, but only the shape evolution of a droplet interacting with turbulent-like flow, this
204 drawback is reasonable.

205 The initial turbulent carrier flow is generated through single phase simulation with a linear forcing scheme
206 [Rosales and Meneveau, 2005, Duret et al., 2012]. This initial forcing is held during 5 eddy turnover, in order
207 to obtain a statistically steady state. Then, a fully-resolved solid particle is added on the domain. This particle
208 ensures a no slip/no penetration condition on a spherical region. After 1 eddy turnover time, the solid constraint
209 is relaxed and the particle is transformed into a droplet. This initialization process avoids any nonphysical shear
210 flow at the interface at start. The droplets are thus initially spherical. The statistics are recorded after an eddy
211 turnover time, T_e , and snapshots are obtained at every $T_e/10$. In this series of simulation, half of the droplets
212 are studied maintaining the turbulence forcing, and, the other half are studied in a decaying turbulence. This
213 method has been used in two previous studies [Chéron et al., 2019, Chen et al., 2019]. In this configuration,
214 approximately 4000 droplets are studied.

215 In order to generate this wide database, the mesh resolution is kept relatively low, 64^3 . To have an accurate
216 representation of morphological evolution, the number of cells across a droplet diameter is set to 32, $d_d =$
217 $32\Delta x$. It gives a cubic box of $L = 1.5 \times 10^{-4} [m]$ and a droplet diameter of $d_d = 7.5 \times 10^{-5} [m]$. The physical
218 configuration is set to $\rho_l/\rho_g = 1$ and $\mu_l/\mu_g = 1$, giving a Reynolds number of $Re = \sqrt{\bar{k}}L/\nu = 15.73$, with k ,
219 the turbulent kinetic energy equal to $\bar{k} = 3.6 [m^2.s^{-2}]$. The surface tension is the only physical parameter that
220 varies in this database. The motivation is to have several Weber numbers generating different droplet shapes.
221 The surface tension variation goes from $\sigma = [6.75 \times 10^{-5}, \dots, 6.75 \times 10^{-1}] [kg.s^{-2}]$, giving a range of Weber
222 number from $We = \rho\bar{k}L/\sigma = [10^{-2}, \dots, 10^2]$. The droplet morphological evolution goes from small surface
223 variation toward highly elongated droplets. To illustrate the typical situations, the visualization of 4 droplets is
224 given in the appendix B.

225 As it will be seen later, the droplets in this database are mostly spherical. Thus, these droplets can charac-
226 terize the deformation due to turbulence in the secondary atomization area.

227 2.4 Droplets generated from airblast atomization

228 In order to obtain droplets close to those observed near the injector, a second numerical experiment is done.
229 The experiment chosen is a planar airblast atomizer that produces several droplets shapes through different
230 breakup mechanisms. By nature, this atomization process is anisotropic. For this reason, one can expect that,
231 statistically, the projection of the droplets in each direction does not provide the same results. Here, three
232 directions are considered for projection: the streamwise direction Z , and, the spanwise directions $X - Y$. The
233 influence of the anisotropy on the shape parameters is studied later in §4.2.

234 The airblast considered here is based on the already studied numerical configuration [Cordesse et al., 2020].
235 The injected liquid has a density of $\rho_l = 12.25 [kg.m^{-3}]$, and, a dynamic viscosity of $\mu_l = 1.11 \times 10^{-4} [Pa.s]$.
236 The density ratio and the viscous ratio, with respect to the carrier phase, are $\rho^* = 10$ $\mu^* = 6.10$. The ratio of
237 injection height against the surface length is 1.25%, momentum ratio is $\frac{\rho_l V_{inj}^2}{\rho_g V_{carrier}^2} = 6.65 [-]$, Weber number
238 is $We_{inj} = \frac{\rho_l^* V_{inj}^2}{\sigma} = 20904 [-]$. The simulation has been performed on 1024 processors. The mesh size is
239 set to $\Delta x = 103, 13 [\mu m]$. The droplet collection is done after 0.2 seconds of atomization once the statistically
240 steady state is reached. The simulation covers 0.13 seconds with a snapshot taken every 2.2×10^{-3} seconds.
241 The droplets are individually studied using the algorithm presented in §2.2. More details can be found in
242 [Belhadef et al., 2012, Cordesse et al., 2020].

243 A snapshot of the airblast is given in figure 4 (left). This figure is obtained applying the projection of the
244 liquid phase over the $X - Z$ plane, perpendicular to the stream-wise direction. As observed, the atomization
245 process generates a wide poly disperse spray. Then, a filter depending on the numerical resolution of the
246 droplets is used to avoid analyzing inaccurate droplets since the computation of morphological parameters is
247 subject to large errors for underresolved droplets [Chéron et al., 2019]. A droplet with an equivalent radius
248 smaller than 2 mesh size, i.e. $R_{EQ,3D} < 2\Delta x$, is then not included in the database. In addition, a filter based on
249 the aspect ratio α_{3D} is applied. Only the droplets with an aspect ratio larger than $\alpha_{3D} > 0.2$ are studied. That
250 allows to remove the large ligaments and also the liquid core. Both filters are illustrated in the morphological-
251 size map shown in figure 4 (right). Through these filters, the analysis covers 40% of the total structures (green
252 kept, red filtered, figure 4 (right)). That corresponds to 1200 droplets. In this figure, different snapshots of the
253 liquid core can be observed, they are located at $R_{EQ,3D} \sim 45$.

254 In this database the limit $\alpha_{3D} = 1$ is not reached, implying that the population of droplets is far from
255 spherical droplets. This database is then a perfect complement to isotropic database presented in §2.3.

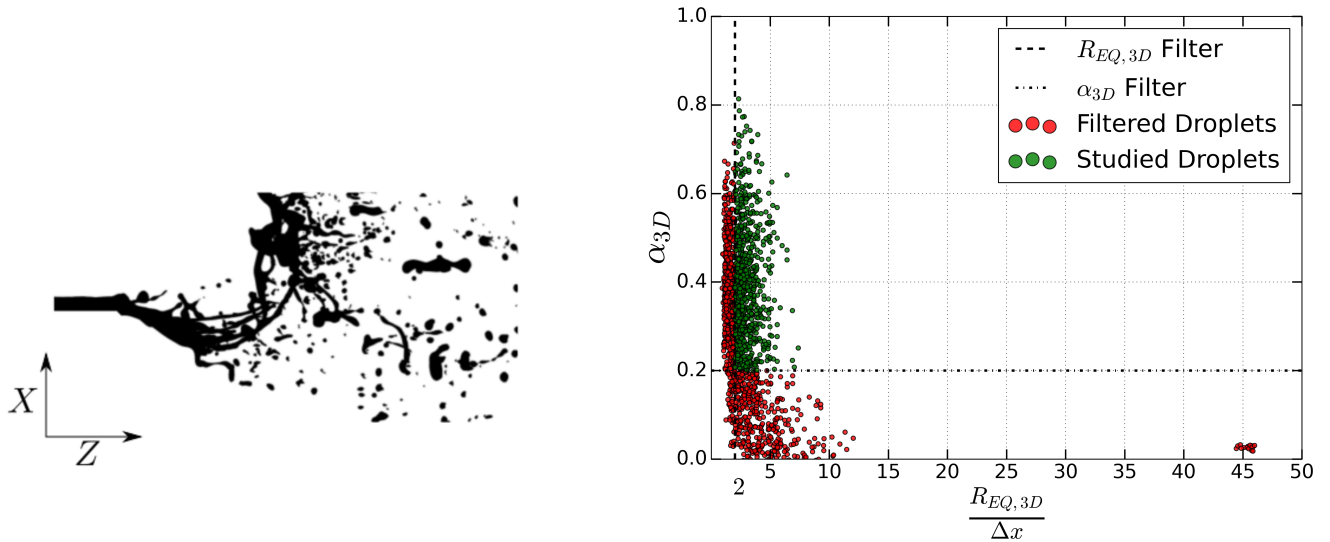


Figure 4: Left: $X - Z$ projection of the liquid volume fraction at a given time step in the airblast atomizer numerical experiment. Right: droplets database from the airblast atomizer based on their aspect ratio, α_{3D} , and numerical resolution, $\frac{R_{EQ,3D}}{\Delta x}$.

256 3 On the spheroid assumption

257 As mentioned, a droplet shape can take different aspect that should need as many shape parameters to be
 258 thoroughly described. From a practical point of view, a reduced set of shape families are considered. The first
 259 one, in terms of relevance to spray analysis, is the spheroid shape, also called ellipsoid of revolution. A droplet
 260 close to the spherical shape can be considered as a spheroid. Spheroids can be classified in two distinct families;
 261 named prolate (cigar-like) and oblate (pancake-like). Each family represents a specific atomization process,
 262 i.e. the prolate case is observed when a sphere is flattened under the action of aerodynamic forces whereas
 263 the oblate case is observed when a droplet undergoes a large drift velocity, relatively to the surrounding gas
 264 [Green, 1975, Clift et al., 1978]. Spheroid shapes can also be associated to the surrounding gas turbulence
 265 properties, as mentioned by [Mukherjee et al., 2019] : "*Axial strain tends to stretch droplets into prolate*
 266 *ellipsoids (cigar-like objects), while bi-axial strain would shape them into oblate ellipsoids (flat pancake-like*
 267 *objects)*". In the absence of other effects than the surface tension and the kinetic forces, these two shapes are
 268 observed since following the Lamb's theory, a spheroidal-like droplet oscillates between oblate and prolate
 269 shape [Lamb, 1881]. In the latter theory, the shapes are not described in terms of spheroid but in terms of
 270 spherical harmonics. Based on these observations, the effect of the projection on the shape parameters of the
 271 droplets under the spheroidal shape assumptions is explored in the present section.

272 3.1 Morphological parameters under spheroid assumption

273 To assess the assumption of considering droplets as spheroids, called hereafter the *spheroid assumption*, re-
 274 lations between shape parameters are derived for the oblate and prolate spheroids. For 2D parameters, the
 275 following analytical relations (Eqs 1-3) were derived for an ellipse by [Blaisot and Yon, 2005] for unifor-
 276 mity, irregularity and SDS parameters as function of the aspect ratio where the approximation of the ellipse
 277 circumference given by [Peano, 1887] is used for the irregularity parameter:

$$\eta_{2D}^E(\alpha_{2D}) = \frac{1 - \alpha_{2D}}{\sqrt{\alpha_{2D}}}, \quad (1)$$

$$\iota_{2D}^E(\alpha_{2D}) = \left(\frac{3(1 + \alpha_{2D})}{4\sqrt{\alpha_{2D}}} - \frac{1}{2} \right)^{-1}, \quad (2)$$

$$\psi_{2D}^E(\alpha_{2D}) = \frac{4}{\pi} \left[\arcsin \left(\sqrt{\frac{1}{1 + \alpha_{2D}}} \right) - \arcsin \left(\sqrt{\frac{\alpha_{2D}}{1 + \alpha_{2D}}} \right) \right]. \quad (3)$$

280 A criterion based on these relations, in the form of a given tolerance, defines a domain in the shape parameter
 281 space that they have called the "elliptic shape family". This is used to estimate the deviation of a droplet shape
 282 from an ellipse, since a droplet whose shape parameters are outside this domain is regarded as not ellipsoidal.
 283 Since the projection of a 3D spheroid is a 2D ellipse (see details later in §3.3), the aforementioned relations
 284 are later extended to a 3D definition. These relations can be used to estimate the deviation of the droplet from
 285 a spheroid using a combination of 3D shape parameters. In this context, it is necessary to distinguish the
 286 prolate and the oblate families, since it modifies the analytical relationship between the parameters. Indeed,
 287 the prolate shape is defined by $a_{3D} = \lambda_1 > \lambda_2 = b_{3D}$ and the oblate shape by $a_{3D} = \lambda_2 > \lambda_1 = b_{3D}$ where
 288 λ_1 is the semi-axis along the symmetry axis and λ_2 is the perpendicular semi-axis. Thus, the volume of a
 289 spheroid, $V = \frac{4}{3}\pi\lambda_2^2\lambda_1$, or the equivalent radius, $R_{EQ,3D} = (\lambda_2^2\lambda_1)^{1/3}$, have a different expression in terms of
 290 a_{3D} and b_{3D} , depending on the spheroid family. With this in consideration, the analytic relation for uniformity,
 291 irregularity and SDS 3D parameters are derived as functions of the aspect ratio, for prolate and oblate spheroid
 292 families:

$$\eta_{3D}^P(\alpha_{3D}) = \frac{1 - \alpha_{3D}}{\alpha_{3D}^{2/3}}, \quad (4)$$

$$\eta_{3D}^O(\alpha_{3D}) = \frac{1 - \alpha_{3D}}{\alpha_{3D}^{1/3}}, \quad (5)$$

$$l_{3D}^P(\alpha_{3D}) = \frac{2\alpha_{3D}^{-2/3}}{1 + \frac{\arcsin(\sqrt{1-\alpha_{3D}^2})}{\alpha_{3D}\sqrt{1-\alpha_{3D}^2}}}, \quad (6)$$

$$l_{3D}^O(\alpha_{3D}) = \frac{2\alpha_{3D}^{2/3}}{1 + \frac{\alpha_{3D}^2}{\sqrt{1-\alpha_{3D}^2}} \operatorname{arctanh}\left(\sqrt{1-\alpha_{3D}^2}\right)}, \quad (7)$$

$$\psi_{3D}(\alpha_{3D}) = 2\sqrt{\frac{\left(1 - \alpha_{3D}^{2/3}\right)^3}{1 - \alpha_{3D}^2}}. \quad (8)$$

293

294 It can be noticed that SDS parameter, based on volume information, does not depend on the spheroid fam-
 295 ily. Following the work of [Blaisot and Yon, 2005], the relations given by Eqs. 5-8 are used to assess the
 296 ellipse/spheroid assumption.

297 3.2 Analysis of the numerical droplet database

298 The 3D shape parameter distribution are compared to the oblate and prolate family curves (Eqs. 5-8) in figure
 299 5, for the droplets generated from isotropic and anisotropic numerical experiments. It is recalled that only the
 300 droplets verifying $\alpha_{3D} > 0.2$ are considered.

301 Values for uniformity parameter η_{3D} (figure 5a) mostly belong to the range $[\eta_{3D}^O, \eta_{3D}^P]$ (upper script are
 302 used to represent the oblate spheroid and prolate spheroid shapes, respectively. In this article, the letter Q is
 303 used to represent both prolate and oblate spheroids when the distinction is not done). As η_{3D} mainly depends
 304 on the primary lengths a_{3D} and b_{3D} , i.e. on two particular points in the contour, this shape parameter is not
 305 strongly related to the true shape of a droplet, i.e. many droplets of different shapes and similar size can share
 306 the same values of a_{3D} and b_{3D} and the same uniformity parameter value. Thus, one can always find a spheroid
 307 \mathcal{S}_P for given a_{3D} and b_{3D} values. Out of range values, i.e $\eta_{3D} < \eta_{3D}^O$ or $\eta_{3D} > \eta_{3D}^P$, are due to $R_{EQ,3D}$ that can
 308 be significantly different from the one of the spheroid \mathcal{S}_P for any droplet. The large range of values spanned by
 309 uniformity between oblate and prolate families makes it a good candidate for classifying spheroids. However,
 310 for the reason mentioned just above, the value pair (α_{3D}, η_{3D}) is not sufficient to identify a droplet as a spheroid
 311 as these two parameters depends manly on the sole primary parameters a_{3D} and b_{3D} .

312 Irregularity parameter l_{3D} depends on area primary parameters, and is thus more strongly related to the
 313 shape of a droplet than η_{3D} . The values are broadly scattered around the prolate curve $l_{3D}^P(\alpha_{3D})$ (see figure 5b),
 314 suggesting that droplets in the numerical database are mainly of the prolate family. Nevertheless, to establish a

315 rigorous shape classification only one shape parameter is not sufficient but a combination of parameters must
316 be used in order to define an effective criterion.

317 The SDS parameter ψ_{3D} is defined from volume-based primary parameters and as such it is strongly related
318 to the true shape of a droplet, as is ι_{3D} . It can be observed on figure 5c that the values covered by ψ_{3D} span
319 largely over the spheroid curve, particularly for low aspect ratios, for the anisotropic set. Thus it can be
320 guessed that this numerical set is not composed only of spheroid droplets. In contrast, the isotropic set clearly
321 shows spheroid-like characteristics for SDS parameter. Moreover, irregularity and uniformity parameter values
322 present also spheroid-like characteristics for this set.

323 It can be concluded from this first simple analysis of the shape parameter values that the anisotropic
324 set presents a wider variation of shapes than the isotropic set. The isotropic set seems mainly composed of
325 spheroid-like droplets whereas the anisotropic set includes also non-spheroid droplet. As an example of the
326 different cases, the droplets of appendix B are highlighted with four different symbols in figure 5. Droplets A
327 and B are the less distorted droplets, i.e. for all morphological parameters the values are closed to the analytical
328 spheroid relations. Droplets C follows the prolate spheroid relation for the uniformity, η_{3D} , and irregularity
329 ι_{3D} . However, this droplet is far from the unic spheroid relation in the case of the SDS parameter ψ_{3D} . The
330 most distorted one, droplet D, also follows the prolate spheroid relation for the first two morphological param-
331 eters. Also, the analysis of the SDS parameter against the aspect ratio, figure 5c, shows a good agreement with
332 the spheroid relation. This is not expected when considering the rendering proposed in appendix B, showing
333 the necessity to consider the shape analysis with several morphological parameters.

334 The 2D parameters obtained from the projection along the three main axes of the computation domain are
335 now considered. These parameters are compared to the analytic relations for the elliptic shape given by Eqs. 1-
336 3. The result of these comparisons is given in figure 6 for both isotropic and anisotropic databases. Isotropic
337 projections are represented in black and the anisotropic projections are colored with respect to the direction of
338 projection, X (red), Y (blue) and Z (green).

339 The same conclusion can be drawn from the observation of the three figures, i.e. the droplets of the isotropic
340 set remain closer to the spheroid family than those of the anisotropic set. This is verified for projections of
341 distorted droplet from the isotropic set, see the projections of droplet D from appendix B on figure 6. It is also
342 noticeable the different behavior of the projection along the Z axis compared to the two other direction for the
343 anisotropic set.

344 From the 3D and 2D analyses, it can be conclude that the population of droplets in the two numeric sets

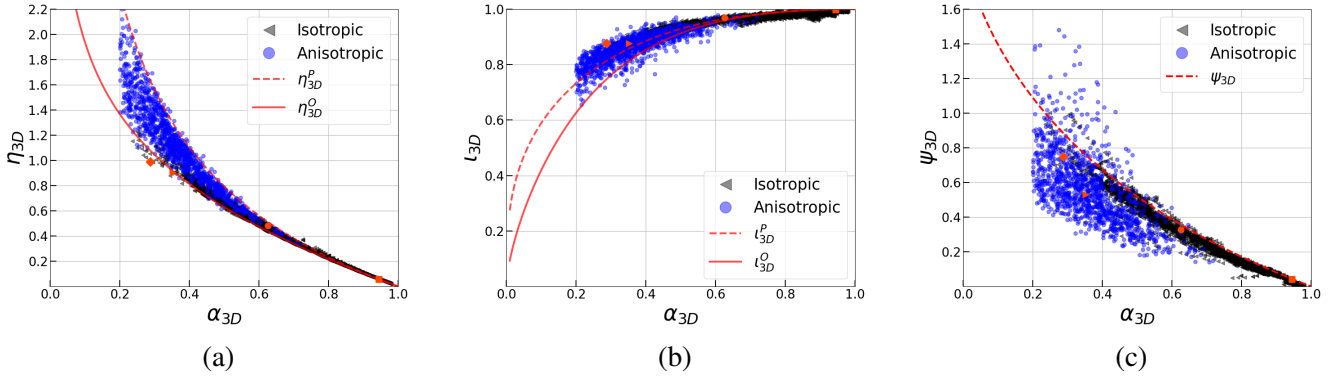


Figure 5: 3D morphological parameters as a function of the aspect ratio, respectively from left to right: the uniformity η_{3D} (figure 5a), irregularity l_{3D} (figure 5b), and SDS parameter ψ_{3D} (figure 5c). Results of the isotropic and anisotropic flows are represented with black triangles and blue circles, respectively. Analytical relations are showed in dashed red line for prolate spheroids, and continuous red line for oblate spheroids. The four droplets extracted from appendix B are represented with square, circle, diamond and down triangle symbols, from A to D, respectively.

345 is not composed of spheroid-like droplets only. In the next subsection the effect of the projection on the
 346 calculation of 2D morphological parameters is explored for spheroids. The uniformity parameter is selected
 347 since it does not permit to classify the morphological shape of an object alone. This parameter is therefore
 348 investigated in detail in this study because the conclusions drawn for this parameter are likely to be extrapolated
 349 to other morphological parameters more representative of the droplet shape, for instance the irregularity or
 350 the SDS parameters. Then, the extension of the uniformity analysis to other parameters is considered as a
 351 perspective.

352 3.3 Projection of spheroids

353 The main goal of this section is to estimate the systematic bias in shape analysis performed on 2D images,
 354 introduced by the projection effect. This is done considering 3D spheroids of known properties. A spheroid is
 355 defined by its symmetry axis, \vec{e}_z , and two lengths; λ_1 the semi-axis length along \vec{e}_z and λ_2 the semi-axis length
 356 perpendicular to \vec{e}_z . As mentioned in §3.1, $\lambda_1 = a_{3D}$ and $\lambda_2 = b_{3D}$ for a prolate spheroid and $\lambda_1 = b_{3D}$ and
 357 $\lambda_2 = a_{3D}$ for an oblate spheroid, a_{3D} and b_{3D} being the maximum and minimum distances from the centroid
 358 to the object surface, respectively. The projection of a spheroid is an ellipse, and, due to the axisymmetry, the
 359 ellipse properties depend only on the angle θ between \vec{e}_z and the projection direction (normal to the projection
 360 plane) (see figure 7).

The ellipse is defined by two lengths, $\lambda_{1,2D}$ and $\lambda_{2,2D}$, that corresponds to the two axis. These lengths can

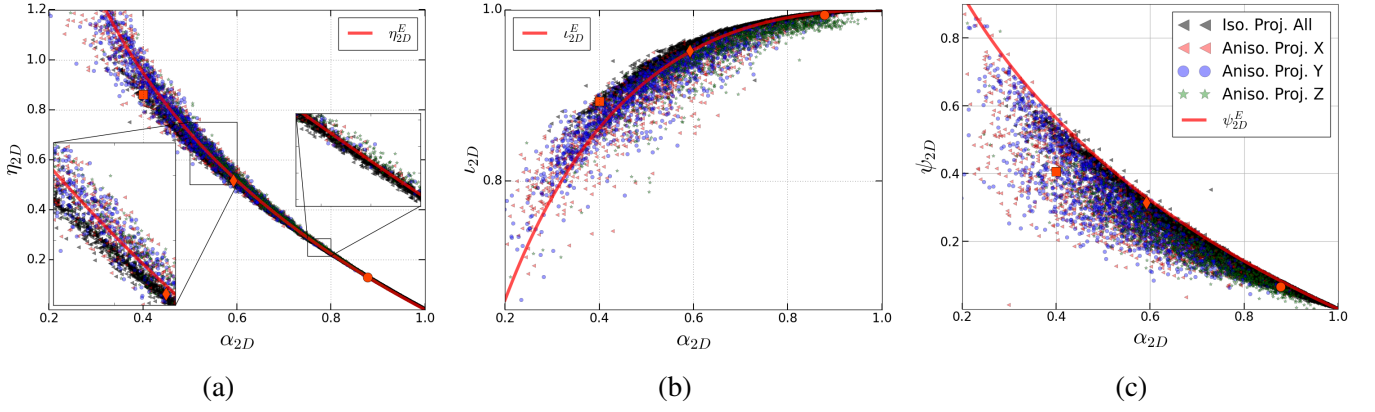


Figure 6: 2D morphological parameters as a function of the aspect ratio, respectively from left to right; the uniformity η_{2D} (figure 6a), irregularity l_{2D} (figure 6b), and SDS parameter ψ_{2D} (figure 6c). Results for the anisotropic flow are plotted with color markers based on the direction of projection and black marker are used for isotropic flow. Analytical relations for the ellipse are shown in solid red line. The X-Y-Z directions of projection of droplet D from appendix B are represented with square, circle and diamond symbols, respectively.

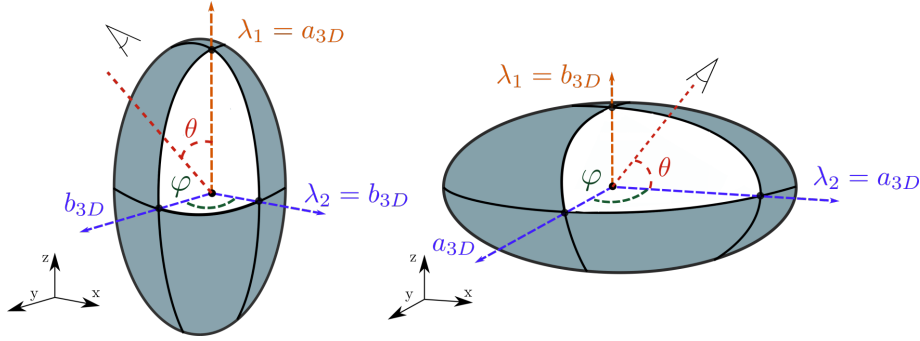


Figure 7: Prolate and oblate spheroids (left and right). θ is the polar or projection angle and φ the azimuthal angle. The lengths λ_1 and λ_2 are the length along the axisymmetry axis and its perpendicular.

be computed from the projection of the ellipse:

$$\lambda_{1,2D} = \frac{\lambda_1 \lambda_2}{\sqrt{\lambda_2^2 \sin^2(\theta) + \lambda_1^2 \cos^2(\theta)}}, \quad (9)$$

$$\lambda_{2,2D} = \lambda_2. \quad (10)$$

These two lengths provide the maximum and minimum distances from the centroid to the contour of the 2D projected ellipse,

$$a_{2D} = \lambda_{1,2D}, \quad (11)$$

$$b_{2D} = \lambda_{2,2D} = \lambda_2 = b_{3D}, \quad (12)$$

for the prolate spheroids, and

$$a_{2D} = \lambda_{2,2D} = \lambda_2 = a_{3D}, \quad (13)$$

$$b_{2D} = \lambda_{1,2D}, \quad (14)$$

for the oblate spheroids.

Expressions for $a_{2D}(\theta)$ and $b_{2D}(\theta)$ depends on the spheroid family (prolate or oblate). These equations obviously shows that $a_{2D} \neq a_{3D}$ and $b_{2D} \neq b_{3D}$ for any projection angle but $\theta = \pi/2$. For $\theta = 0$, corresponding to a projection axis parallel to \vec{e}_z , the projection is a disk leading to $a_{2D} = b_{2D} = \lambda_2$.

The variation of $a_{2D}(\theta)$ and $b_{2D}(\theta)$ is illustrated in figure 8 for two spheroids, one prolate and one oblate, of same major semi-axis $a_{3D} = 1$ and of same uniformity $\eta_{3D} = 0.25$. The 2D equivalent radius $R_{EQ,2D} = \sqrt{a_{2D}b_{2D}}$ is also plotted and compared to $R_{EQ,3D} = (\lambda_2^2\lambda_1)^{1/3}$ (see §3.1) in this figure. It is recalled that the projection area of a spheroid is an ellipse. Two additional equivalent radii are proposed here: $R_{EQ,2D,O} = (b_{2D}a_{2D}^2)^{1/3}$ for a presumed oblate droplet and $R_{EQ,2D,P} = (a_{2D}b_{2D}^2)^{1/3}$ for a presumed prolate droplet. Whatever the spheroid family, a_{2D} and b_{2D} vary between a_{3D} and b_{3D} . One can also remark that for all angles: $b_{2D} = \lambda_2 = b_{3D}$ for prolate spheroids and $a_{2D} = \lambda_2 = a_{3D}$ for oblate spheroids. It can be observed in figure 8 a bell curve for the 2D equivalent radii for a prolate, and, the inverse bell curve for an oblate object. For both spheroid cases, the equivalent radius $R_{EQ,2D}$, evolves below and above $R_{EQ,3D}$. For the prolate spheroid, the additional radius for a presumed prolate droplet $R_{EQ,2D,P}^P \leq R_{EQ,3D}$, the equality being reached for $\theta = \pi/2$. For the oblate spheroid the radius for a presumed oblate droplet $R_{EQ,2D,O}^O \geq R_{EQ,3D}$ and here again equality is reached for $\theta = \pi/2$. For the prolate spheroid $R_{EQ,2D,O}^O$ is always greater than $R_{EQ,2D}$. It can be noticed that whatever the spheroid family $R_{EQ,2D,P}^P \leq R_{EQ,2D} \leq R_{EQ,2D,O}^O$. This property is used below.

The error on the estimation of the primary lengths, a_{2D} , b_{2D} and $R_{EQ,2D}$ with respect to the 3D values, described in this section, has an influence on the shape parameters obtained from the projection step (2D from 3D).

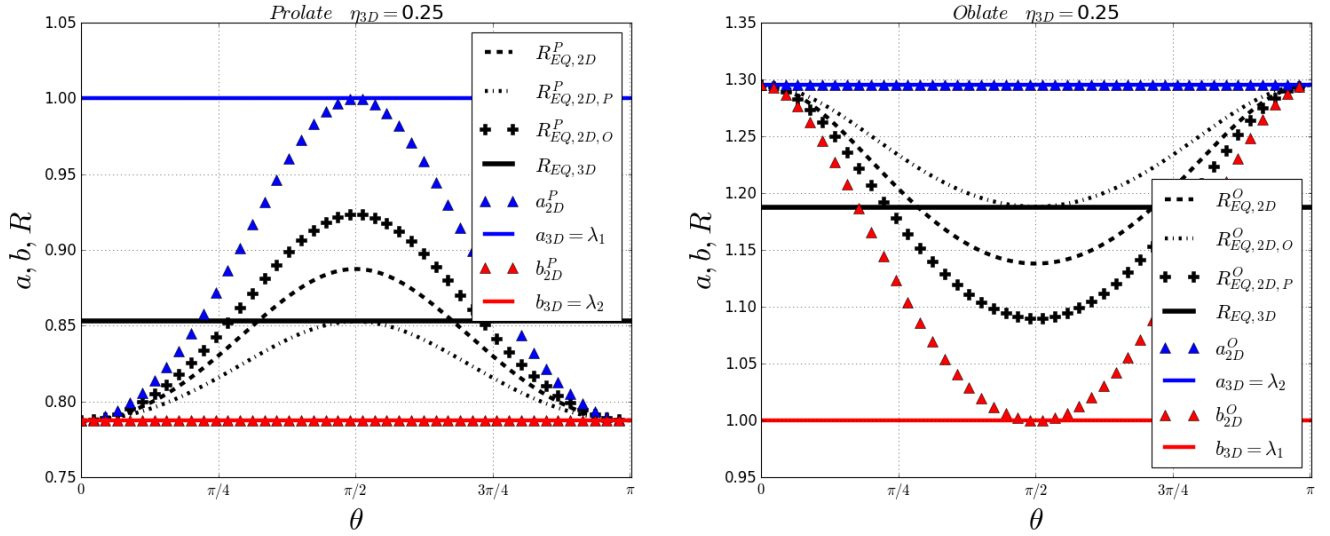


Figure 8: Evolution of a_{2D} , b_{2D} , $R_{EQ,2D}$ and $R_{EQ,2D}^P$ or $R_{EQ,2D}^O$ against π for a spheroid with an initial uniformity parameter of $\eta_{3D} = 0.25$, left: prolate spheroid, right: oblate spheroid. Limits of the 3D spheroid are given: a_{3D} , b_{3D} , and $R_{EQ,3D}$.

3.4 Deviation on uniformity computation due to projection under the spheroid assumption

In this section, the potential deviation of 2D uniformity parameter η_{2D} from the real 3D value η_{3D} is evaluated. It is recalled that uniformity is defined by λ_1 , λ_2 and the equivalent radius. Oblate and prolate spheroid families are considered separately and the evolution of η_{2D} is analyzed as a function of the direction of projection, θ . To illustrate the main trends, the curves for $\eta_{2D}(\theta)$ is shown in figure 9 for the two spheroids considered in §3.3. Two extra uniformity parameters are also introduced: $\eta_{2D,P}^Q$ is the value obtained for a presumed prolate droplet and $\eta_{2D,O}^Q$ is the one for a presumed oblate droplet for a prolate, or oblate spheroid, respectively O and P upper script (it is recalled that to simplify the notation, the upper script letter Q represents both oblate and prolate families). In the definition of these extra uniformity, $R_{EQ,2D}$ is replaced by the corresponding $R_{EQ,2D,Q}^Q$. The main points to retain are: (i) η_{2D}^Q and $\eta_{2D,Q}^Q$ curves have a bell shape whatever the spheroid family; (ii) minimum value for η_{2D} equal zero whatever η_{3D} for both spheroid families (corresponding to $\theta = 0$ and $\theta = \pi$, i.e. projection equal to a disk); (iii) maximum value for $\eta_{2D,Q}^Q$ equal η_{3D} (for $\theta = \pi/2$) when the right spheroid family is presumed (in this case, 2D and 3D values for a , b and $R_{EQ,2D,Q}^Q$ are equal, see figure 8).

From the previous remarks it can be concluded that the most probable situation is that the 2D uniformity obtained from a projection underestimates the 3D uniformity. To analyze this deviation from a statistical point of view, the 2D uniformity is averaged over all observation orientations, i.e. over solid angle 4π sr. Each

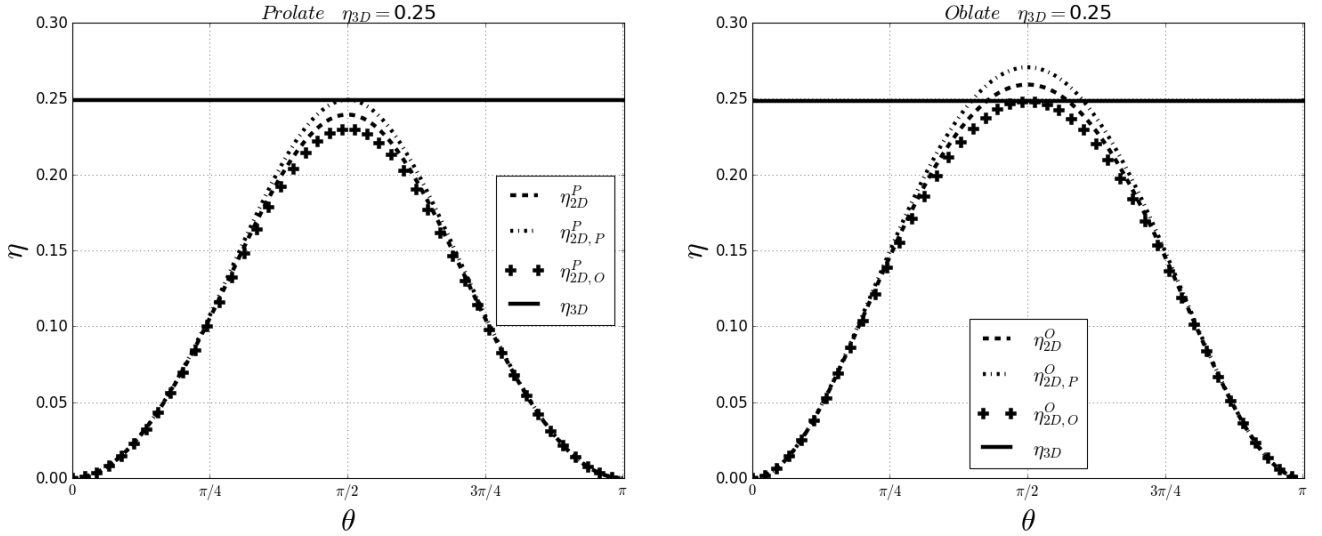


Figure 9: Evolution of the 2D uniformity, η_{2D}^P or η_{2D}^O , and the corrected 2D uniformity, $\eta_{2D,P}^Q$ and $\eta_{2D,O}^Q$ with Q depending on the initial family, for a range of direction of projection $\theta = [0, \pi]$. The 3D uniformity value is fixed, $\eta_{3D} = 0.25$, left: prolate spheroid, right: oblate spheroid.

398 observation direction is assigned a probability $\frac{\sin \theta}{4\pi} d\theta d\varphi$ where φ is the azimuthal angle. Averaged expression
 399 are thus given by:

$$\bar{\eta}_{2D} = \int_0^\pi \frac{a_{2D}(\theta) - b_{2D}(\theta)}{R_{EQ,2D}(\theta)} \frac{\sin(\theta)}{2} d\theta, \quad (15)$$

400 and

$$\bar{\eta}_{2D,Q} = \int_0^\pi \frac{a_{2D}(\theta) - b_{2D}(\theta)}{R_{EQ,2D,Q}(\theta)} \frac{\sin(\theta)}{2} d\theta. \quad (16)$$

401 The analytical derivation of these integrals are developed in Appendix A. To illustrate the relation between 2D
 402 and 3D values of the uniformity parameter, a plot of η_{3D} vs η_{2D} is shown in figure 10 for a random set of oblate
 403 spheroids and a random set of prolate spheroids (each set consists of 4000 elements). For each set, the points
 404 $(\eta_{2D,O}^P, \eta_{2D,O}^O, \eta_{3D})$ and $(\eta_{2D,O}^P, \eta_{2D,P}^P, \eta_{3D})$ are also drawn. The curves for the mean values $\bar{\eta}_{2D}^P$ and $\bar{\eta}_{2D}^O$
 405 are also plotted in figure 10 for both prolate and oblate spheroids as function of η_{3D} . The following information
 406 can be deduced:

- 407 • averaged 2D uniformity values ($\bar{\eta}_{2D}^Q$) generally underestimates the 3D value, except for $\bar{\eta}_{2D}^O > \eta_{3D}$ with
 408 $\eta_{3D} > 1.2$ for the oblate family. That is even the case when considering the alternative equivalent radius
 409 $\eta_{2D,O}^O$ and $\eta_{2D,P}^P$.
- 410 • The minimum value for η_{2D}^Q is always 0 (a circular shape can be observed even for very deformed
 411 spheroids, as in the case of the projection of deformed prolates, see figure 3). Nevertheless, for larger

412 values of η_{3D} the probability to observe a circle decreases.

- 413 • The maximum value of the shape-assumed 2D uniformity $\eta_{2D,max,Q}^Q$ is equal to η_{3D} for the well presumed
- 414 shape.
- 415 • The maximum 2D uniformity $\eta_{2D,max}^Q$ underestimates (overestimates) η_{3D} for the prolate (oblate) spheroids.

416 The estimation of the 2D uniformity parameter with the assumption of the wrong family is also added

417 to figure 10. These values are obtained applying the oblate assumption (i.e. using $R_{EQ,O}^P$ in the definition

418 of η_{2D}^P) for the prolate spheroids, and vice versa. The miss-assumption of the spheroid family drastically

419 modifies the deviation between 2D and 3D uniformity parameters, compared to the right assumption. For the

420 prolate spheroids, $\eta_{2D,O}^P$ is shifted toward lower values of 2D uniformity, which increases the deviation with 3D

421 values. For the oblate case, the results are also worsened since the population is shifted toward higher values of

422 uniformity, resulting in a stronger overestimation of the 3D value. This figure also shows that regardless of the

423 initial spheroid family, the oblate assumption never overestimates the 3D value for the uniformity parameter.

424 This will be helpful for the analysis of the isotropic and anisotropic databases (see §4.1 and 4.2 respectively)

425 where the representation of η_{3D} vs η_{2D} is also used to analyze both droplet databases.

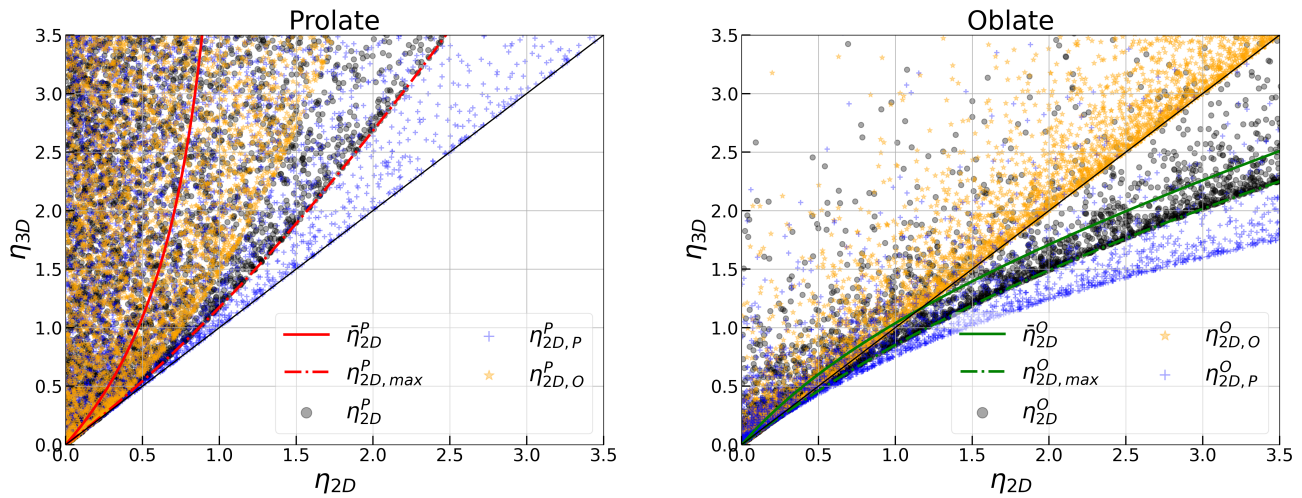


Figure 10: Plots of η_{3D} vs η_{2D} . Lines: 2D averaged uniformity for each kind of spheroid family (prolate: $\bar{\eta}_{2D}^P$, oblate $\bar{\eta}_{2D}^O$), and maximum values (lower script *max*). Markers: random spheroids sets without (grey circles η_{2D}^P or η_{2D}^O) and with spheroid family correction (blue cross for prolate $\eta_{2D,P}^P$ and $\eta_{2D,P}^O$, and orange star for oblate $\eta_{2D,O}^P$ and $\eta_{2D,O}^O$). Left figure: prolate spheroid set. Right: oblate spheroid set.

4 Shape parameter deviation analysis for numerical databases

The deviation in shape parameter estimation induced by 2D projection is analyzed here for two numerical databases, i.e. the isotropic database presented in §4.1 and the anisotropic one presented in §4.2. It is reminded that the isotropic database corresponds to droplets deformed by isotropic turbulence (e.g. secondary atomization area), and the anisotropic database to droplets with a large drift velocity (e.g. primary atomization area). For each database, the length-type primary parameters are first considered before the uniformity shape parameter.

4.1 Isotropic database

The isotropic database has been introduced in §2.3. It results from a simulation of an isolated droplet of constant size, i.e. monodisperse droplet population, in a developed Homogenous Isotropic Turbulence-like flow. For this reason, the projections are independent of the direction of projection.

4.1.1 Length-type primary parameters

The uniformity shape parameter is based on three length-type primary parameters: the equivalent radius R_{EQ} and the maximal and minimal distances to the droplet centroid (a and b). The deviation resulting from the projection on a 2D plane of the 3D droplet contour is first estimated for these three quantities.

First, 2D and 3D equivalent radii are compared. In the isotropic database, all the droplets have the same initial volume (and thus, the same $R_{EQ,3D}$). Equivalent radius without assumption $R_{EQ,2D}$, with prolate spheroid assumption $R_{EQ,2D,P}$, and with oblate spheroid assumption $R_{EQ,2D,O}$ are considered. These 2D equivalent radii are scaled by $R_{EQ,3D}$ for simplification purpose. The probability distribution functions (PDFs) for the three normalized 2D equivalent radius are plotted in figure 11. The radii obtained from the projection in the three orthogonal directions of the Cartesian mesh of the numerical domain are considered for each droplet. The distribution is constructed with 35 bins. The distributions are Gaussian-like with the following average values:

$$\left[\frac{R_{EQ,2D}}{R_{EQ,3D}} \right] = 1.011, \quad \left[\frac{R_{EQ,2D,P}}{R_{EQ,3D}} \right] = 0.953, \quad \left[\frac{R_{EQ,2D,O}}{R_{EQ,3D}} \right] = 1.043,$$

and standard deviations:

$$\sigma \left(\frac{R_{EQ,2D}}{R_{EQ,3D}} \right) = 0.066, \quad \sigma \left(\frac{R_{EQ,2D,P}}{R_{EQ,3D}} \right) = 0.071, \quad \sigma \left(\frac{R_{EQ,2D,O}}{R_{EQ,3D}} \right) = 0.080.$$

441 showing that the best estimate of $R_{EQ,3D}$, that would give a distribution centered on $R_{EQ,2D}/R_{EQ,3D} = 1$ with
 442 low dispersion, is given by $R_{EQ,2D}$ on average. The prolate assumption underestimates the radius while the
 443 oblate assumption overestimates it.

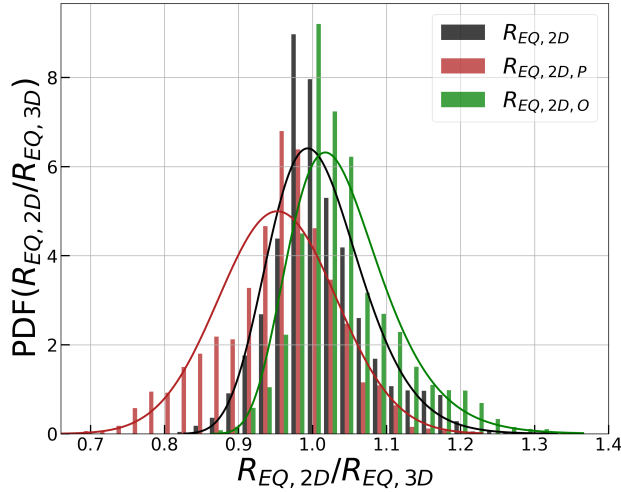


Figure 11: Probability density functions for $R_{EQ,2D}$ in black, $R_{EQ,2D,P}$ in red (prolate spheroid assumption) and $R_{EQ,2D,O}$ in green (oblate spheroid assumption).

444 It can be noticed that as the three directions of projection are considered. For a given droplet, any under-
 445 estimation or overestimation of $R_{EQ,3D}$ in one direction is offset by the projection in the other two directions.
 446 This basic observation has an important impact on the calculation of the maximal and minimal distances that
 447 is now analyzed.

448 The comparison between 2D and 3D values for a and b , is presented in figure 12. These length-type
 449 parameters are also scaled by $R_{EQ,3D}$ to simplify the presentation in a way to obtain normalized values lower
 450 than 1, i.e. $b/R_{EQ,3D}$ and $R_{EQ,3D}/a$. A colormap is used to classify the points according to the value of
 451 $R_{EQ,2D}/R_{EQ,3D}$. As explained before, for droplets with $R_{EQ,2D}/R_{EQ,3D} \simeq 1$, an accurate estimation of a and
 452 b lengths is expected.

453 The lengths a_{2D} and b_{2D} should be in the range $[b_{3D}, a_{3D}]$, implying points below the first bisector line in
 454 figure 12. This is almost verified, the points above the first bisector are due to computational inaccuracies.

455 The points near to the first bisector mainly correspond to $R_{EQ,2D}/R_{EQ,3D} \simeq 1$. That concerns spherical

456 droplets (e.g. droplet (A) in appendix B), or elongated droplets projected in a direction that minimizes the
 457 error.

458 A correlation between the overestimation of $R_{EQ,3D}$ and the overestimation of b_{3D} is clearly seen from
 459 the colored points in figure 12 left. In other words, if the minimal distance is not correctly captured by the
 460 projection, the equivalent radius is overestimated. This situation can be illustrated by droplet C) of appendix
 461 B. A correlation between the underestimation of $R_{EQ,3D}$ and the underestimation of a_{3D} is also seen from the
 462 colored points in figure 12 right, i.e. if a_{3D} is underestimated, then, the equivalent radius is also underestimated
 463 (dark blue markers in the figure).

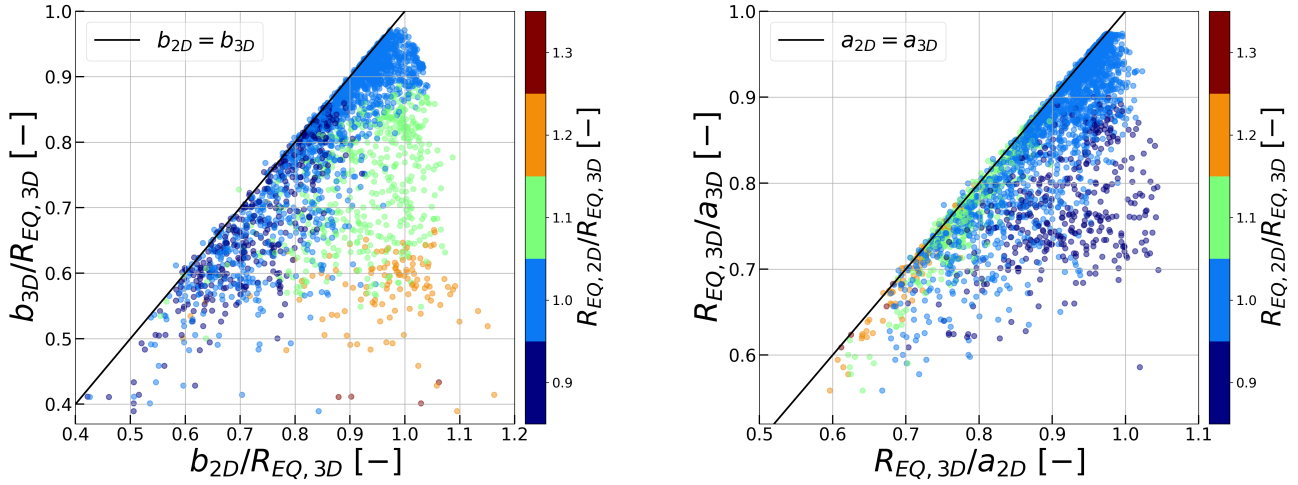


Figure 12: Distribution of b_{3D} against b_{2D} scaled by the equivalent 3D radius $R_{EQ,3D}$ (left). Distribution of a_{3D} against a_{2D} scaled by the equivalent 3D radius $R_{EQ,3D}$ (right). The color map is associated to $R_{EQ,2D}/R_{EQ,3D}$ values, see figure 11.

464 4.1.2 Uniformity shape parameter projection analysis

465 The plot of η_{3D} vs η_{2D} for the isotropic set is shown in figure 13. The analytic maximum and averaged
 466 curves for η_{2D} with and without spheroid family assumption, are included for the oblate and prolate families,
 467 respectively in green and red, and the markers are colored by $R_{EQ,2D}/R_{EQ,3D}$ values but no spheroid shape
 468 assumption is made to estimate η_{2D} . It is recalled that a 3D droplet creates three 2D information, based on the
 469 three Cartesian direction of projection.

470 This figure is to compare to the figure 10 (in particular black circles that corresponds to projection without
 471 assumption) keeping in mind that the range of values for η is reduced here. As markers only fill the space over
 472 the first bisector, it is guessed that the spray is mainly populated by prolate-like spheroids. Also, this does not

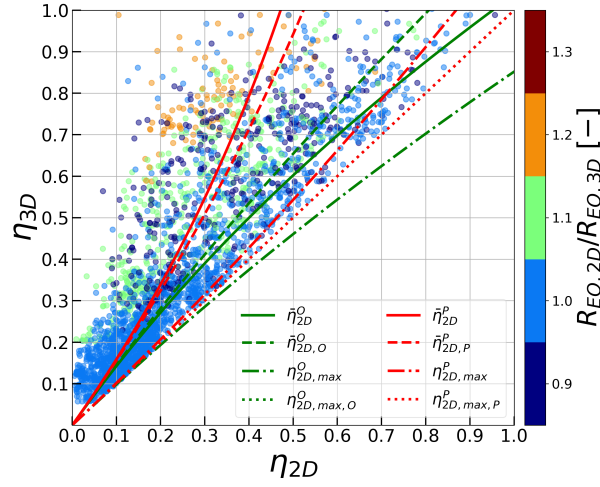


Figure 13: Distribution of the 3D uniformity, η_{3D} , against η_{2D} . The color map is associated to $R_{EQ,2D}/R_{EQ,3D}$ values, see figure 11. Lines: 2D averaged uniformity for each kind of spheroid family, $\bar{\eta}_{2D}^Q$, maximum values, $\bar{\eta}_{2D,max}^Q$, and family correction, $\bar{\eta}_{2D,Q}^Q$ and $\bar{\eta}_{2D,max,Q}^Q$.

473 consider the entire distribution since few points are observed on the right of $\eta_{2D,max}^P$ curve, which can only
 474 be crossed by oblate-like droplets. Generally, the points are centered on the prolate spheroid analytical mean
 475 value; $\bar{\eta}_{2D}^P$, and, limited by the first bisector. One can assimilate the majority of these droplets to prolate-like
 476 spheroids. Finally, in contrast to the theoretical framework, here no perfect circular projections are observed
 477 for large deformed 3D shapes. For instance, the most circular projection for large deformed droplets is droplet
 478 D in appendix 10 that is strongly deformed ($\eta_{3D} = 0.9$) and have a projection in Y direction close to a circle
 479 $\eta_{2D,Y} = 0.13$.

480 The systematic underestimation of the uniformity due to projection can also be understood in terms of pri-
 481 mary lengths projections. A correlation was shown in figure 12 between an overestimation of the minor axis
 482 b and an overestimation of the equivalent radius R_{EQ} . The combination of these two overestimations leads to
 483 underestimate η as can be observed for the orange colored markers in figure 13. A correlation between an un-
 484 derestimation of the major axis a and an underestimation of R_{EQ} was also found. These two underestimations
 485 are likely to be compensated (see the definition of η parameter in table 1). The dark blue colored markers in
 486 figure 13 are indeed a little closer to the first bisector than orange ones.

487 The results presented here show the interest of the analogy with the random projection of spheroids. How-
 488 ever, only isotropic droplets with a low deformation have been treated here. The next section deals with a more
 489 realistic case with anisotropic droplet deformation.

490 **4.2 Anisotropic database**

491 The anisotropic database has been introduced in §2.4 and is constituted of polydisperse droplets. As an indica-
492 tor, the relative span factor is; $RSF = \frac{D_{0,9}-D_{0,1}}{D_{0,5}} = 0.690$. It results from a simulation of airblast atomization
493 with the stream-wise direction along Z axis. For this reason, the projections for each direction are examined
494 individually.

495 **4.2.1 Length-type primary parameters**

496 The PDF for the three 2D equivalent radii (i.e. $R_{EQ,2D}$, $R_{EQ,2D,P}$ and $R_{EQ,2D,O}$) normalized by $R_{EQ,3D}$ are
497 plotted in figure14, for X , Y and Z directions, from left to right, respectively. In contrast to the isotropic
498 database, the volume of the droplets varies.

499 Here also Gaussian-like distributions are observed. The average and standard deviation of these distribu-
500 tions are given in table 2. As observed for the isotropic case, the best estimate of $R_{EQ,3D}$ is given by $R_{EQ,2D}$;
501 the prolate assumption globally underestimates the equivalent radius whereas the oblate estimate globally over-
502 estimates it.

503 It can be clearly seen that the X and Y projections produce similar statistics, meanwhile a different behavior
504 appears on the projection along the streamwise Z direction. Moreover, results for X and Y directions are
505 similar to the ones for the isotropic case. For the Z direction, mean values are ordered the same way than for
506 the other two directions but the best estimate is given here by the oblate assumption but with the wider standard
507 deviation.

508 To explain this, let's consider that the droplets are spheroids. Now, in opposition to the theoretical de-
509 velopments on §3.3-3.4, these spheroids have a preferential alignment, the Z direction. Thus, the $R_{EQ,2D}$
510 underestimates or overestimates the $R_{EQ,3D}$ (depending on the prolate or oblate spheroid probability due to
511 the oscillatory regime of these droplets), while the X and Y direction produces more accurate estimation since
512 they capture the lengths along the axisymmetry axis. This ideal case explains the larger dispersion of $\frac{R_{EQ,2D}}{R_{EQ,3D}}$
513 on Z projection. To go further on this assumption based on an ideal droplet shape, since the main value of
514 $\frac{R_{EQ,2D}}{R_{EQ,3D}} = 0.938 < 1$, more prolate spheroids than oblates are present in this database. Indeed, a value higher
515 than one would have yield to a majority of oblate spheroids in the population, as detailed in figure 8. This
516 idealized instance may appear to be a long way from the complexity of the physics behind an airblast atomizer.
517 However, since the droplets are the result of ligament breaking, and the ligaments in this type of atomizer

518 are aligned along the Z axis, this interpretation sounds appropriate. The initial droplets are thus prolate-like
 519 spheroids aligned with the Z axis, which follows the classical oblate/prolate oscillations predicted by linear
 theory and observed in the literature [González and García, 2009, Moallemi et al., 2016].

$\overline{[-]}$	X	Y	Z	$\sigma(-)$	X	Y	Z
$\frac{R_{EQ,2D}}{R_{EQ,3D}}$	1.021	1.010	0.938	$\frac{R_{EQ,2D}}{R_{EQ,3D}}$	0.071	0.0756	0.1244
$\frac{R_{EQ,2D,P}}{R_{EQ,3D}}$	0.898	0.892	0.889	$\frac{R_{EQ,2D,P}}{R_{EQ,3D}}$	0.0847	0.0811	0.1105
$\frac{R_{EQ,2D,O}}{R_{EQ,3D}}$	1.142	1.128	1.025	$\frac{R_{EQ,2D,O}}{R_{EQ,3D}}$	0.1166	0.122	0.1566

Table 2: Mean values and standard deviation of $\frac{R_{EQ,2D}}{R_{EQ,3D}}$ for different computations of $R_{EQ,2D}$, left and right, respectively.

520

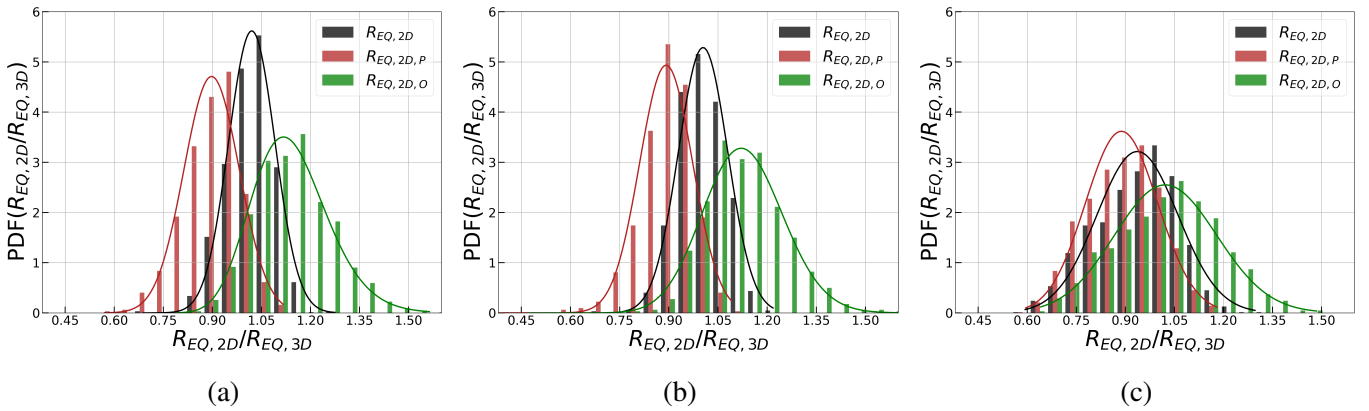


Figure 14: From left to right: histogram of the deviation of the projected equivalent radius: $R_{EQ,2D}$ in black, and their correction based on the prolate spheroid assumption: $R_{EQ,2D,P}$, in red, and for the oblate spheroid assumption: $R_{EQ,2D,O}$, in green, for direction of projections; X (figure 14a), Y (figure 14b), and Z (figure 14c).

521 The minimal and maximal lengths, i.e. a and b , are now considered. The deviation of the 2D to the 3D
 522 versions of these primary parameters, scaled by $R_{EQ,3D}$, is shown in figure 15 for X , Y and Z projection
 523 directions, respectively from left to right, with a parameter in bottom row and b parameter in top row. A color
 524 map based on $R_{EQ,2D}/R_{EQ,3D}$ values is used to color the marker points, as in the isotropic section and the first
 525 bisector is also drawn to clearly identify $a \simeq b$ cases.

526 A correlation between the overestimation of $R_{EQ,3D}$ and the overestimation of b_{3D} as well as between the
 527 underestimation of $R_{EQ,3D}$ and the underestimation of a_{3D} is observed, as for the isotropic case (see the color
 528 distribution in figure 15 which is particularly clear for Z direction (right column)). It is recalled that the PDF
 529 for $R_{EQ,2D}/R_{EQ,3D}$ along Z direction shows a larger dispersion (see figure 14 and table 2). Also, the results
 530 observed for the X and Y directions are in the range of the isotropic set.

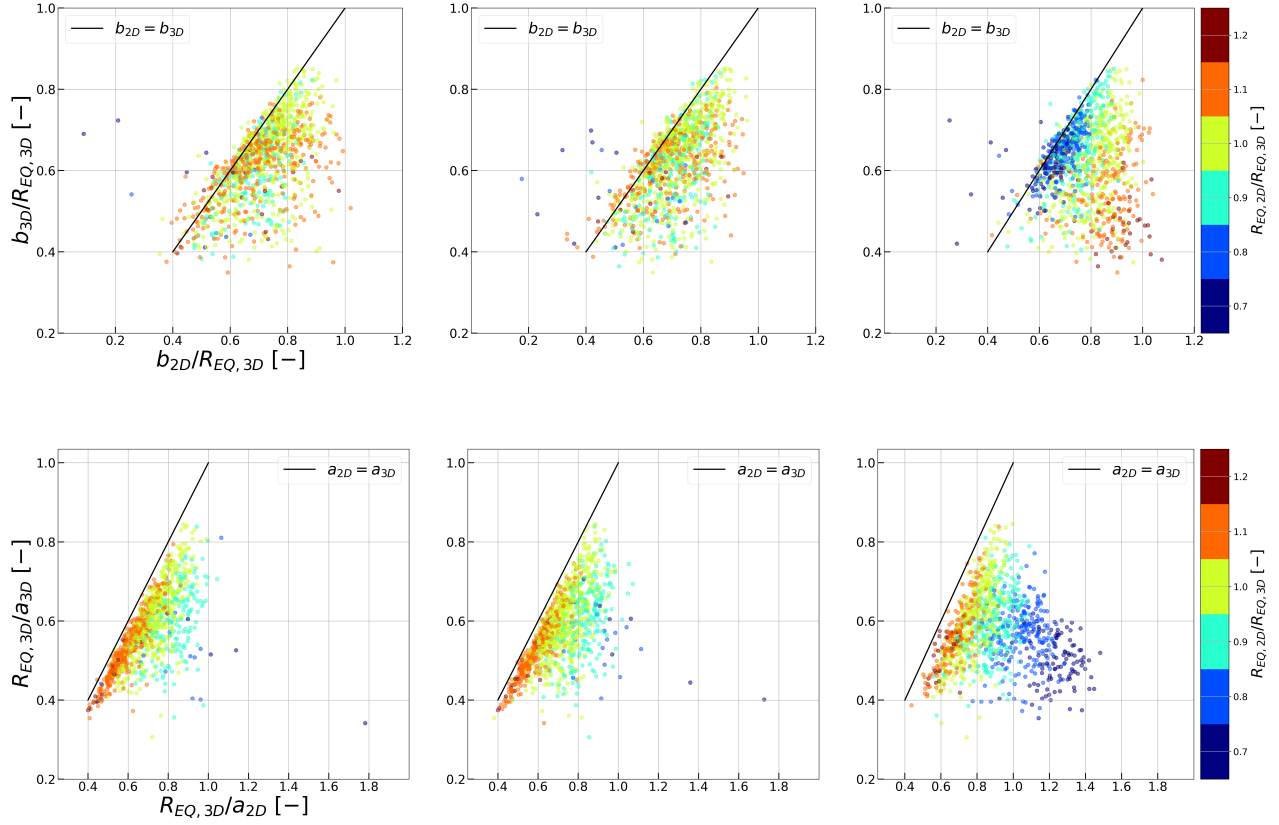


Figure 15: Distribution of b_{3D} against b_{2D} scaled by the equivalent 3D radius $R_{EQ,3D}$ (top). Distribution of a_{3D} against a_{2D} scaled by the equivalent 3D radius $R_{EQ,3D}$ (bottom). The color map is based on the scaling of the equivalent 2D and 3D radius, see figure 14. An individual scattering of each direction of projection is given for both quantities; from left to right: X-Y-Z.

531 Few points recover $a_{2D} = a_{3D}$, and are located on the first bisector. The length b_{2D} retrieves the 3D
 532 value for several points in the set but the probability that the projection allows to recover the 3D value is not
 533 correlated to the ratio $R_{EQ,2D}/R_{EQ,3D}$, in opposition to the isotropic set. Another divergence with this database
 534 is the observation of minimal lengths overcoming the 3D value; $b_{2D} > b_{3D}$. These droplets are consistent since
 535 $b_{2D} < R_{EQ,2D} < a_{2D}$. Also, they are far from a spheroidal shape, and the centroid of their projection is shifted
 536 which explains this overestimation of the minimal length with respect to the 3D droplet.

537 4.2.2 Uniformity shape parameter projection analysis

538 The deviation analysis of the uniformity parameter, η_{3D} vs η_{2D} , is shown in figure 16 with X, Y and Z projec-
 539 tion directions from left to right, respectively. The same colormap as the one in figure 15 is used to classify the
 540 points according to the value of $R_{EQ,2D}/R_{EQ,3D}$. The range of values for η is almost the double than for the
 541 isotropic database. For projections along X and Y the points are mainly located in the 'prolate' assumption

542 zone, i.e. η_{2D} is evenly distributed in the range $[\bar{\eta}_{2D}^P/2, \eta_{2D,max}^P]$. This shows a systematic underestimation of
 543 the uniformity value, increasing for higher η_{3D} . For Z direction, the points are shifted towards lower values
 544 of η_{2D} with values approaching the limit $\eta_{2D} = 0$. From the observations of section §4.2.1 and the uniformity
 545 analysis, it is confirmed that the majority of droplets are prolate-like aligned along the Z direction. In other
 546 words, an observer looking at the spray in the streamwise direction will see many circular shapes. As discussed
 547 before, for these very cases the equivalent radius (here dark blue markers) is underestimated.

548 It can be shown that the analytic average value $\bar{\eta}_{2D}^P$ for a random set of prolate spheroids (see §3.3) is
 549 overestimated for X and Y directions and underestimated for Z directions. This confirms that the orientation
 550 of observation has a great influence on shape parameter estimation from 2D projection, which is almost always
 551 the case in experiments.

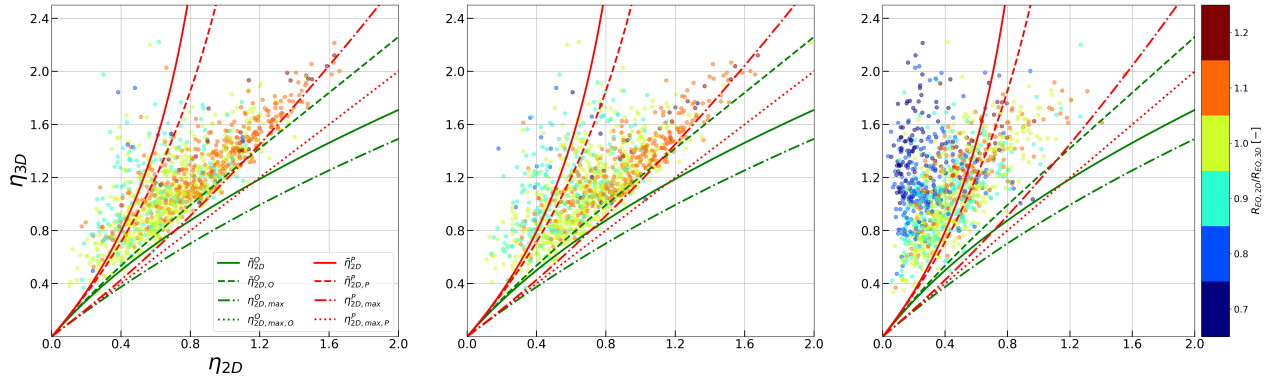


Figure 16: Distribution of the 3D uniformity, η_{3D} , against η_{2D} , for the three direction of projections, left to right: $X - Y - Z$. Lines: 2D averaged uniformity for each kind of spheroid family, $\bar{\eta}_{2D}^A$, maximum values, $\bar{\eta}_{2D,max}^Q$, and family correction, $\bar{\eta}_{2D,Q}^Q$ and $\bar{\eta}_{2D,max,Q}^Q$ (it is recalled that Q represents both prolate and oblate spheroid shapes). The color map scales equivalent 2D and 3D radius, see figure 14.

522 5 Application of the correction on 2D droplets from experimental database

523 5.1 Experimental setup

524 The experimental database is obtained from a set of more than one hundred images recorded on a water/air
 525 spray produced by a shear-coaxial injector [Ficuciello et al., 2017]. The injection condition is characterized by
 526 $We_g = \frac{\rho_g U_g^2 D_l}{\sigma} = 400$, and $Re_l = \frac{\rho_l U_l D_l}{\mu_l} = 6600$, where ρ_g and U_g are the density and the bulk velocity of the
 527 gas, ρ_l , U_l , and μ_l are the density, the bulk velocity and the viscosity of the liquid, and σ the surface tension
 528 between liquid and gas.

559 An example of image of the experiment is shown in figure 17 where a large view of the flow is also
 560 displayed. Objects not totally included in the image (i.e. touching an image side) are rejected as well as very
 561 big objects (with a projected area greater than the one of a circle of about 2 mm in diameter). A filter based
 562 on the contrast of the image is applied ($\mathcal{C} > 0.1$), removing objects with a low SNR (signal-to-noise ratio).
 563 Another filter based on the estimation of the point spread function is also applied to select droplets in a given
 564 range of out-of-focus, whatever their size (see [Blaisot and Yon, 2005] or [Fdida et al., 2010]). The database
 565 contain around 30000 droplets corresponding to about 300 droplets per image. In figure 18 the size probability
 566 density functions based on the 2D equivalent radius are plotted for the raw data and after filter application.
 567 Undoubtedly, this filter concerns mainly the small droplets. Filtering these droplets modifies the relative span
 568 factor from 3.755 to 2.458.

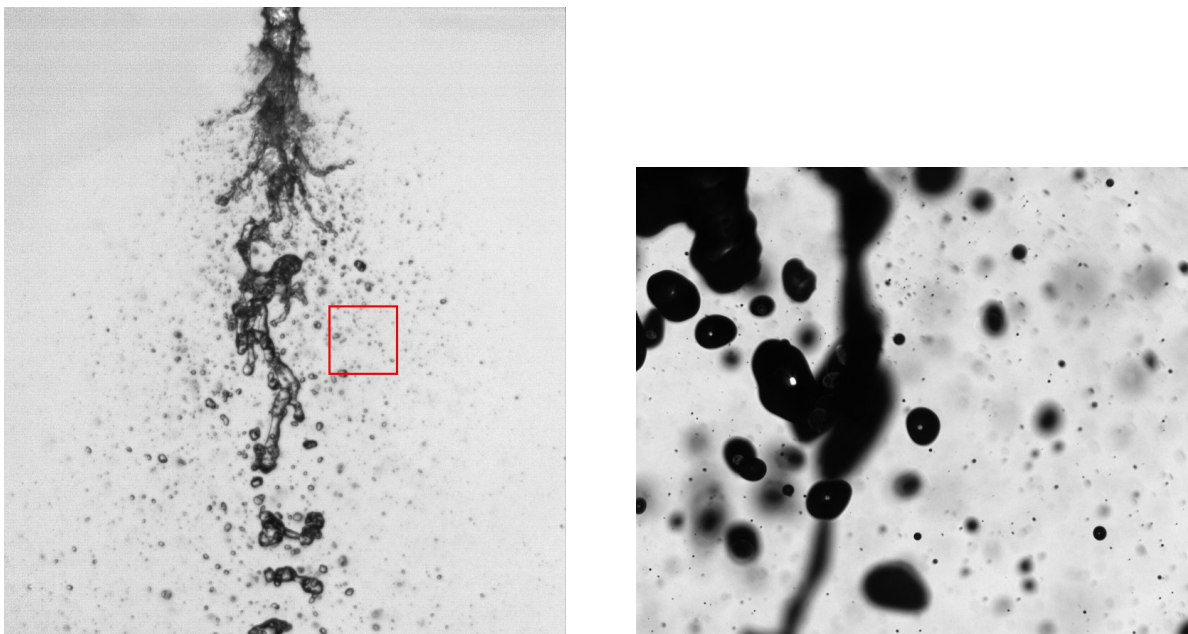


Figure 17: Images of the spray: Air-assist jet on the left and an image of the experimental database on the right. The red rectangle shows the region covered by images of the database.

569 5.2 Elliptic assumption

570 Two-dimensional uniformity (η_{2D}), irregularity (ι_{2D}), SDS (ψ_{2D}) and aspect ratio (α_{2D}) parameters are ex-
 571 tracted from the experimental database. The distribution of the three first parameters (η_{2D} , ι_{2D} , ψ_{2D}) as func-
 572 tions of the aspect ratio (α_{2D}) are compared to the elliptic shape relations (Eqs. 1-3) in figure 19. Markers are
 573 colored using a three classes color map based on the equivalent radius $R_{EQ,2D}$.

574 The smallest droplets (blue markers) are almost close to the elliptic shape curves (red lines). This is not

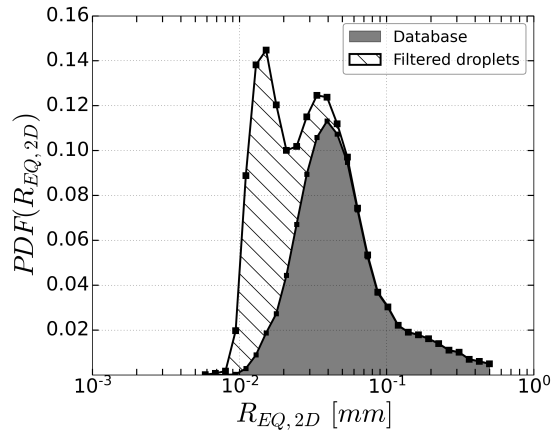


Figure 18: Droplet size distribution of the experimental database. Data removed by applying the out-of-focus filters/morphological filter correspond to the hashed zone.

575 surprising since these droplets are the most likely to keep a near spherical shape. It can be observed that a large
576 number of big droplets (orange and red markers) are far under the elliptic curve for ι parameter (see figure 19b).
577 Indeed, due to their size, these droplets are prone to large deformation. Only a few big droplets are away from
578 the elliptic curve for uniformity parameter (see the region near $(\alpha_{2D}, \eta_{2D}) = (0.2, 1.3)$ in figure 19a). Thus,
579 this parameter is neither able to identify spheroid-like droplet in its 2D version nor in its 3D one. Also, a certain
580 amount of large droplets are away from the elliptic curve for ψ parameter (figure 19c) but a more restraining
581 filter that combines these three morphological parameters must be considered to recover object with elliptic-
582 like projections only [Blaisot and Yon, 2005, Fdida and Blaisot, 2008]. These distributions are quite similar
583 to the ones shown in figure 6 for the numerical databases. In particular, the X and Y projections for the
584 anisotropic numerical database (Airblast simulation) seems close to the experiment database distributions.
585 The main differences come from the larger deformation observed in the experiment. This is because the
586 experiment indicates a larger range of droplet sizes. Also, the smallest structures are not recovered in the
587 numerical simulations due to low resolution imposed by the numerical restriction (see [Herrmann, 2010a] for
588 a discussion of this point).

589 5.3 Analysis of the uniformity deviation

590 In the experiments, the 3D parameters are not available. It was shown in §3 that the range and the mean values
591 for η_{2D} can be estimated for a population of spheroids randomly oriented with a given value for η_{3D} . The
592 relation between η_{3D} and $\bar{\eta}_{2D}$ given in Eq. 20 (developed in appendix A and showed as a red solid line in figure
593 10) can be used to recover 3D parameter values from 2D measurements. Applying this specific equation for

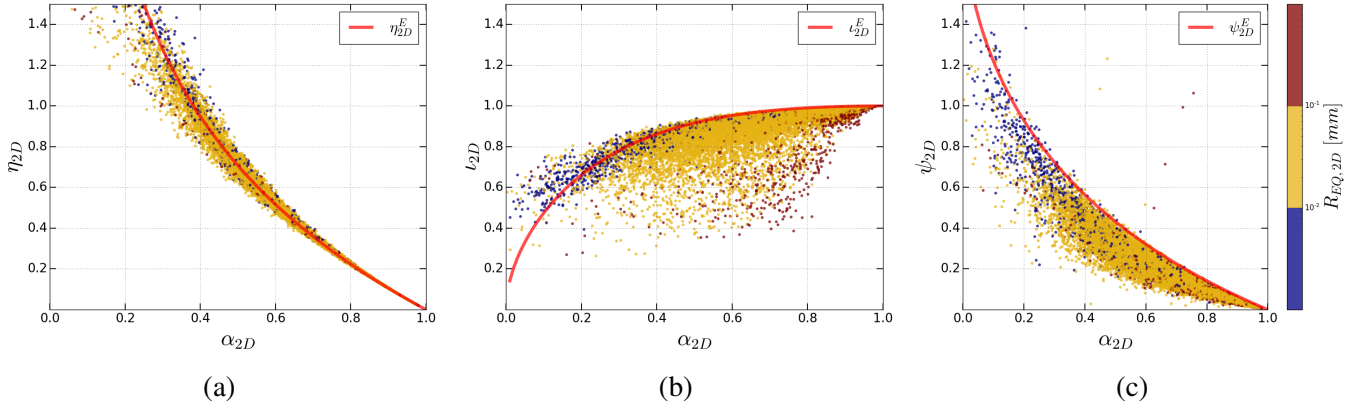


Figure 19: Morphological parameters as a function of the 2D aspect ratio, respectively from left to right the uniformity η_{2D} (figure 19a), irregularity l_{2D} (figure 19b), and SDS parameter ψ_{2D} (figure 19c). Analytical relations are showed in solid red line. The color map is based on the equivalent 2D radius expressed in logarithmic scale

594 the reconstruction implies three assumptions: (i) the droplets are prolate spheroids; (ii) the main axis of the
 595 spheroids is randomly oriented; (iii) the distribution of η_{3D} is a Dirac function. The two first assumptions have
 596 been discussed extensively in §3 and §4. The last one is treated here. For a given distribution of η_{3D} and under
 597 assumptions (i) and (ii), there is only one distribution of η_{2D} but the inverse is not true. From the numerical
 598 database, η_{3D} was estimated from the value of η_{2D} and the relation given by Eq. 20. This provides a mean
 599 value of 2.13 for the estimated η_{3D} whereas the real 3D mean value is given by $\bar{\eta}_{3D} = 1.15$. Furthermore, the
 600 estimation of η_{3D} from η_{2D} parameter values of the experimental database leads to outlier about 190. To assess
 601 more realistic values for η_{3D} from η_{2D} measurements, an alternative approach is proposed, based on equivalent
 602 radii and the probability density function for uniformity parameter.

603 The uniformity parameter is determined from the primary parameters a_{2D} , b_{2D} and $R_{EQ,2D}$ (see §1.2). For
 604 each droplet, the prolate and oblate assumptions are made to determine the corresponding values for η_{2D}^Q (see
 605 §3.3). A plot of η_{2D}^Q vs η_{2D} is shown in figure 20a for the experimental and numerical databases (isotropic and
 606 anisotropic). For the three databases, the sets of points are evenly distributed around the mean $\bar{\eta}_{2D}^Q$, obtained
 607 from a set of randomly oriented spheroids (see §4). As expected, $\eta_{2D,O}^Q \leq \eta_{2D} \leq \eta_{2D,P}^Q$, since the prolate
 608 assumption gives a lower value of the equivalent radius whereas the oblate assumption gives a bigger one. The
 609 probability density function of η_{2D} and η_{2D}^Q (for prolate and oblate assumptions) are given in figure 20b. The
 610 PDFs follow a log-normal distribution. As expected, the oblate and prolate assumptions shift the distribution to
 611 larger or smaller values of the uniformity, respectively. The PDF of η_{3D} for the anisotropic numerical database
 612 is also represented in figure 20b.

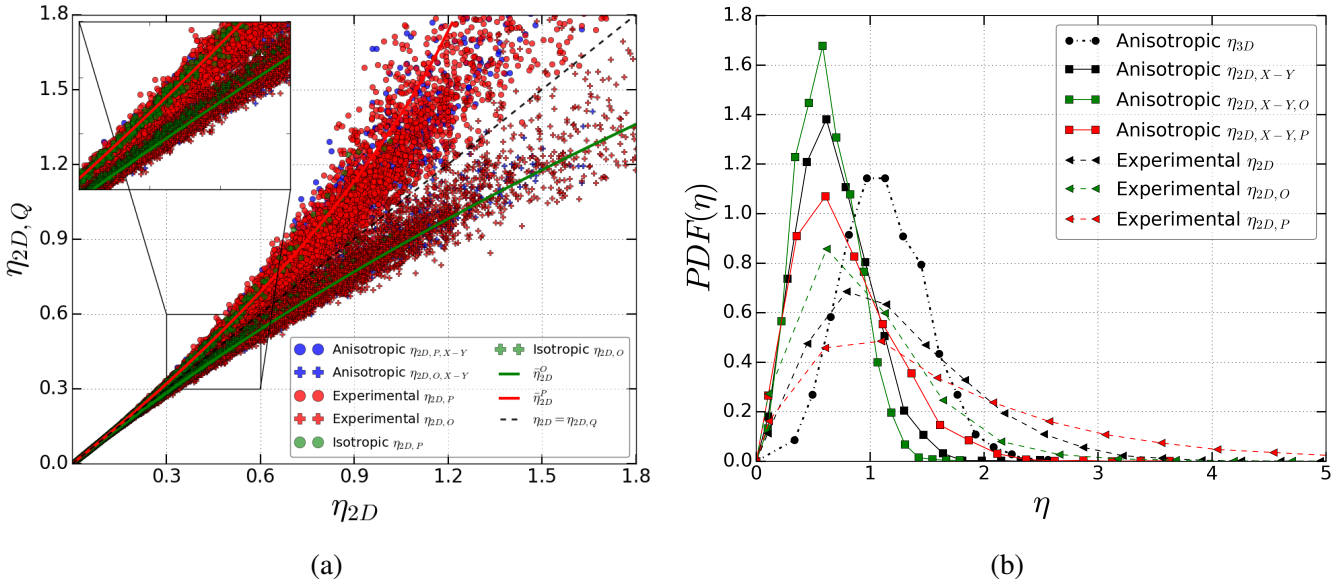


Figure 20: a) η_{2D}^Q vs η_{2D} for prolate (circles) and oblate (crosses) assumptions in the case of isotropic (green), anisotropic (blue) and experimental (red) databases. Solid lines are for $\bar{\eta}_{2D}^Q$ determined on a set of randomly oriented spheroids. b) Probability density function of uniformity (direct and with prolate or oblate assumptions) for each database.

613 The ultimate interrogation of this work is to determine the possibility to estimate a 3D parameter from its
614 2D measurements. The comparison of distributions of η_{2D} and η_{3D} for the anisotropic database clearly shows
615 an underestimation of the 3D parameter by the 2D parameter, described beforehand. The present approach
616 consists in analyzing the statistical properties of the parameter distributions. As commented for the considered
617 databases, the uniformity PDF follows a log-normal distribution: $P(\eta, \sigma, \chi) = \frac{\chi}{\sigma\eta\sqrt{2\pi}} \exp\left(-\frac{\log^2(x/\chi)}{2\sigma^2}\right)$. For
618 instance, the best fit obtained for the numerical anisotropic 3D database, η_{3D} , gives the values of $\sigma = 0.31$ and
619 $\chi = 1.42$, and, is represented in figure 21. This shows an excellent agreement with the pdf of 3D anisotropic
620 uniformity. Under the assumption of a family of spheroid (prolate or oblate), the distribution of the 2D uni-
621 formity can be estimated from the distribution of 3D uniformity and the distribution of angles θ . As seen in
622 §4, the prolate assumption is more appropriate to account for atomizing droplets. From the log-normal fit of
623 η_{3D} distribution and the assumption of prolate droplets, several distributions for η_{2D} were guessed, one for a
624 random distribution of orientation angles θ (corresponding to the distribution $\frac{\sin\theta}{2}d\theta$), and for a fixed angle set
625 to $\theta = [\pi/6, \pi/3, 4\pi/10, \pi/2]$ (corresponding to a Dirac function distribution).

626 As seen in figure 21, the distributions with a fixed angle provides a log-normal like distribution. The
627 obtained distribution is narrower than the measured one (in other words, σ is smaller). The averaged 2D
628 uniformity decreases when increasing the fixed θ angle. The case $\theta = \pi/2$ can be considered as the limit
629 where all the droplets are aligned with the streamwise axis. That is why this angle Dirac distribution over-

630 estimates the measured 2D uniformity. The random distribution shows a completely different behavior. The
 631 distribution is no longer a log-normal.

632 This is linked to the fact that in this case the probability to see a perfect circle after projection is not null,
 633 neither the probability of a null value for η . In practice, this can occur only for a projection along streamwise
 634 Z direction, which is never the case in experiments. This random distribution under-estimated the measured
 635 2D uniformity obtained for $X - Y$ projection (i.e. perpendicular to the streamwise direction). As conclusion,
 636 the random and the fixed angle at $\theta = \pi/2$ distributions surround the true distribution for η_{2D} as observed in
 637 figure 21. A more accurate knowledge of the θ distribution should give a better prediction of the reconstruction
 638 of the distribution for η_{2D} . Here, this distribution has not been computed. The authors consider that it would
 639 be important to include this distribution in future measurements as it will allow a better understanding of the
 640 relationship between the 2D and 3D parameters.

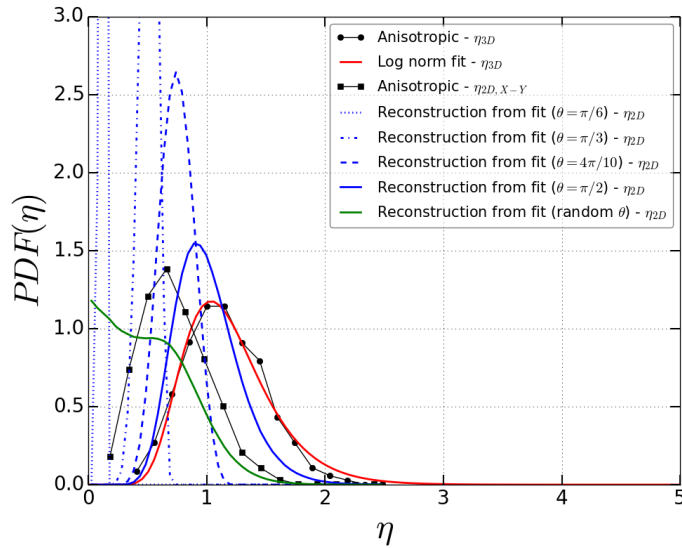


Figure 21: Probability density function of the uniformity of the numerical anisotropic experiment. Reconstruction of 2D are given from 3D.

641 The previous results are encouraging since the shape parameters can be accurately estimated under basic
 642 assumptions. These assumptions should allow the estimation of the probability density function of the 3D
 643 parameters based on 2D parameter distributions. The present results have shown a sensibility to the selected
 644 reconstruction methodology, to go from a 2D distribution to a 3D distribution. Due to the complexity of the
 645 question, an extension of the present communication focusing on the reconstruction of the 3D distribution is
 646 considered by the authors.

647 **6 Conclusion**

648 An accurate characterization of the droplets shape is of main interest to understand the atomization process.
649 This characterization is often done on 2D projections obtained from experimental setups. As seen in the lit-
650 erature [Ghaemi et al., 2009], different shape parameters can be used to describe these droplets' projections.
651 Among the several parameters introduced in the present paper, the uniformity parameter is considered to ana-
652 lyze the deviation of the 2D value from the 3D value. Two approaches are pursued: i) an analytical approach
653 based on the assumption that the droplets are spheroids; ii) a numerical approach were numerical atomized
654 droplets, and their projections, are analyzed.

655 According to these two approaches, the following results are retained:

- 656 • Droplets can be considered as spheroids in order to analyze their shape parameters.
- 657 • For a given 3D shape, the 2D shape parameters can vary depending on the angle of projection. For the
658 uniformity shape parameter, and under the assumption of spheroidal shape, analytical relations between
659 the 2D and 3D parameters are given in §3.4 and appendix A).
- 660 • The kind of spheroid considered (oblate or prolate) modifies strongly the relations between 2D and 3D
661 uniformity parameter. In the present databases, the droplets projections follows the statistical behavior
662 of prolate spheroid. In particular, the 2D uniformity underestimates the 3D uniformity.
- 663 • The projection axis should be considered when analyzing a database. The primary lengths and the
664 shape parameters can suffer from a systematic deviation due to this preferential projection angle. In
665 the anisotropic numerical case studied here, the sketch of prolate-like droplets that are aligned prefer-
666 entially along the injection axis (axis Z) is drawn. As a result, this projection axis exacerbates both
667 the underestimation of the equivalent radius (affecting the size probability distribution function) and the
668 underestimation of the uniformity shape parameter.

669 In experiments, the projection axis is often perpendicular to the injection axis, which improves the estima-
670 tion of 3D parameters. However, certain complex atomization configurations do not permit an optimal optical
671 configuration, which can drastically influence the deviation from the 3D results. In order to show the effect
672 of the projection on the shape parameter analysis, the comparison between an experimental database and the
673 generated numerical databases is done in §5. This comparison shows that the uniformity distributions fit a log-
674 normal distribution. Furthermore, the study of the uniformity distributions provides a tool that should allow us

675 to predict the 3D uniformity distribution from the 2D measured one, considered as an extension of the present
676 communication.

677 The authors are convinced that the true understanding of atomization, and in particular of the transition
678 between primary and secondary atomization, requires a detailed characterization of the 3D droplet shape. This
679 will require in the future more experiments using 2D projections, but also numerical simulations, and, the
680 application of optical measurement methods allowing the 3D reconstruction of the droplet shape.

681 **Acknowledgments**

682 This work was granted access to the HPC resources of IDRIS, TGCC and CINES under the allocation A0092B1010
683 made by GENCI (Grand Equipement National de Calcul Intensif) and the CRIANN (Centre Régional Infor-
684 matique et d'Applications Numériques de Normandie) under the scientific project N. 201 704. The authors
685 would thank Alexandre Poux for the fruitful exchanges. We also thank the Normandy region for their funding
686 of this research.

687 **A Analytical integration of uniformity averages**

688 In this appendix we provide the methodology to obtain the integrals given in equations 15 and 16. For space
 689 reasons, here we develop only the $\bar{\eta}_{2D}$ for prolate spherodids, $\bar{\eta}_{2D}^P$. At the end of this appendix, the solution for
 690 each case is provided.

$$\bar{\eta}_{2D} = \int_0^\pi \frac{a_{2D} - b_{2D}}{\sqrt{a_{2D}b_{2D}}} \frac{\sin(\theta)}{2} d\theta = \int_0^\pi \sqrt{\frac{a_{2D}}{b_{2D}}} \frac{\sin(\theta)}{2} d\theta - \int_0^\pi \sqrt{\frac{b_{2D}}{a_{2D}}} \frac{\sin(\theta)}{2} d\theta \quad (17)$$

691 This equation can be reduced introducing the parameter $\mathcal{A} = \frac{\lambda_2}{\lambda_1}$. First, we consider a prolate spheroid
 692 where this parameter is equal to the aspect ratio $\mathcal{A} = \alpha_{3D} < 1$. In this case the previous equation becomes:

$$\bar{\eta}_{2D}^P = \int_0^\pi \sqrt[4]{\frac{1}{(\mathcal{A}^2 - 1)\sin^2\theta + 1}} \frac{\sin(\theta)}{2} d\theta - \int_0^\pi \sqrt[4]{(\mathcal{A}^2 - 1)\sin^2\theta + 1} \frac{\sin(\theta)}{2} d\theta \quad (18)$$

693 We can reduce the integrals to the interval 0 to $\pi/2$ and multiply by two since $\sin(\theta)$ is symmetric at $\pi/2$.
 694 Thus, making an integral by substitution $u = \sin^2(\theta)$ we obtain:

$$\bar{\eta}_{2D}^P = \frac{1}{2} \int_0^1 \frac{1}{\sqrt{1-u} \sqrt[4]{(\mathcal{A}^2 - 1)u + 1}} du - \frac{1}{2} \int_0^1 \frac{\sqrt[4]{(\mathcal{A}^2 - 1)u + 1}}{\sqrt{1-u}} du \quad (19)$$

695 These integrals can be computed analytically using hypergeometric function ${}_2F_1$. Thus the final solution is
 696 given by:

$$\bar{\eta}_{2D}^P = {}_2F_1\left(\frac{1}{4}, 1; \frac{3}{2}; 1 - \mathcal{A}^2\right) - {}_2F_1\left(-\frac{1}{4}, 1; \frac{3}{2}; 1 - \mathcal{A}^2\right) \quad (20)$$

697 Similar development can be done for the oblate case where $\mathcal{A} = \frac{1}{\alpha_{3D}} > 1$. From Eq. 17, the following
 698 relation is obtained:

$$\bar{\eta}_{2D}^O = {}_2F_1\left(-\frac{1}{4}, 1; \frac{3}{2}; 1 - \mathcal{A}^2\right) - {}_2F_1\left(\frac{1}{4}, 1; \frac{3}{2}; 1 - \mathcal{A}^2\right) \quad (21)$$

699 One can notice that the solution is similar to the prolate since the two integrals are switched.
 Similarly, the development is done for $\bar{\eta}_{2D,P}^P$ and $\bar{\eta}_{2D,O}^O$. The solution is given by:

$$\bar{\eta}_{2D,P}^P = \int_0^\pi \frac{a_{2D} - b_{2D}}{\sqrt[3]{a_{2D}b_{2D}^2}} \frac{\sin(\theta)}{2} d\theta = {}_2F_1\left(\frac{1}{3}, 1; \frac{3}{2}; 1 - \mathcal{A}^2\right) - {}_2F_1\left(-\frac{1}{6}, 1; \frac{3}{2}; 1 - \mathcal{A}^2\right) \quad (22)$$

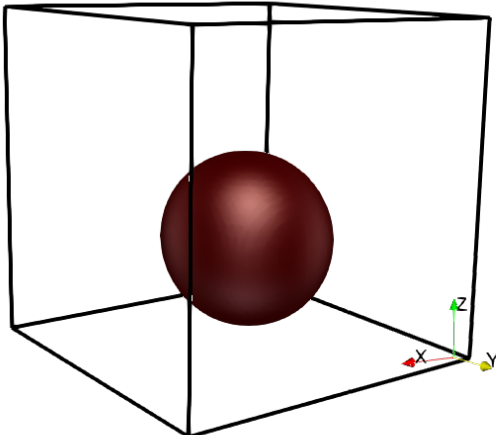
$$\bar{\eta}_{2D,O}^O = \int_0^\pi \frac{a_{2D} - b_{2D}}{\sqrt[3]{a_{2D}^2b_{2D}}} \frac{\sin(\theta)}{2} d\theta = {}_2F_1\left(-\frac{1}{6}, 1; \frac{3}{2}; 1 - \mathcal{A}^2\right) - {}_2F_1\left(\frac{1}{3}, 1; \frac{3}{2}; 1 - \mathcal{A}^2\right) \quad (23)$$

700 **B Influence of the correction on singular droplets from the isotropic**
 701 **database.**

702 In this appendix, four droplets are extracted from the isotropic database, illustrating the influence of the pro-
 703 jection. The lengths and morphological parameters are also given for each droplet. These droplets (A, B, C,
 704 and D), represent 4 different morphological shapes:

- 705 A) Almost spherical droplet.
- 706 B) Slightly deformed droplet.
- 707 C) Bean shape flattened droplet.
- 708 D) Distorted droplet.

709 **B.1 Droplet A)**



710

Figure 22: Almost spherical droplet extracted from the HIT-like flow database.

711

	2D			3D
	X	Y	Z	-
$R_{EQ,3D}/a$	0.975	0.988	0.991	0.972
$b/R_{EQ,3D}$	0.973	0.999	0.987	0.971
$R_{EQ}/R_{EQ,3D}$	0.999	1.01	0.996	-
α	0.949	0.988	0.978	0.944
η	0.053	0.013	0.0225	0.0573
ι	0.999	1.0	1.0	0.998
ψ	0.031	0.007	0.012	0.0407
$R_{EQ,P}/R_{EQ,3D}$	1.008	1.008	1.002	-
η_P	0.0522	0.012	0.023	-
$R_{EQ,O}/R_{EQ,3D}$	0.990	1.004	0.994	-
η_O	0.053	0.013	0.023	-

Table 3: Morphological parameters of the extracted droplet, see figure 22, of the HIT-like flow database.

712 **B.2 Droplet B)**

713

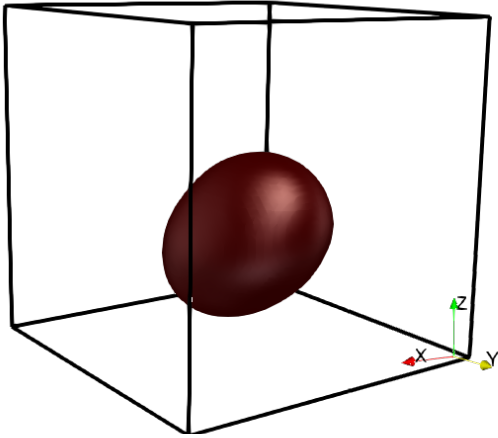


Figure 23: Slightly deformed droplet extracted from the HIT-like flow database.

714

	2D			3D
	X	Y	Z	-
$R_{EQ,3D}/a$	0.804	0.9333	0.83	0.7767
$b/R_{EQ,3D}$	0.837	0.823	0.8893	0.8056
$R_{EQ}/R_{EQ,3D}$	1.050	0.9563	1.0351	-
α	0.673	0.768	0.738	0.626
η	0.387	0.260	0.305	0.482
ι	0.977	0.988	0.985	0.969
ψ	0.218	0.111	0.167	0.327
$R_{EQ,P}/R_{EQ,3D}$	1.090	0.981	1.089	-
η_P	0.373	0.253	0.290	-
$R_{EQ,O}/R_{EQ,3D}$	0.956	0.899	0.984	-
η_O	0.426	0.277	0.321	-

Table 4: Morphological parameters of the extracted droplet, see figure 23, of the HIT-like flow database.

715 **B.3 Droplet C)**

716

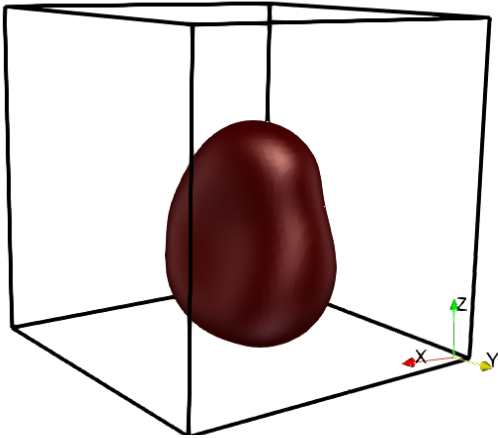


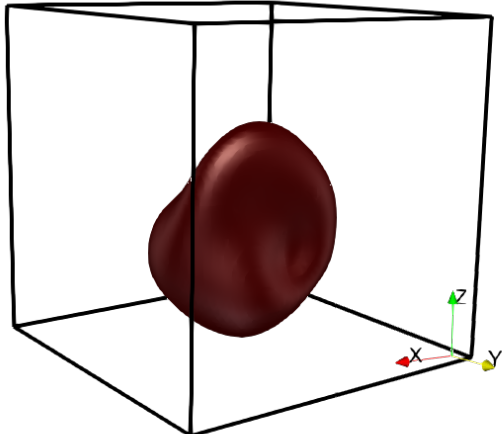
Figure 24: Bean shape flattened droplet extracted from the HIT-like flow database.

717

	2D			3D
	X	Y	Z	-
$R_{EQ,3D}/a$	0.727	0.747	0.857	0.719
$b/R_{EQ,3D}$	1.07	0.587	0.603	0.401
$R_{EQ}/R_{EQ,3D}$	1.236	0.959	0.872	-
α	0.778	0.438	0.516	0.288
η	0.245	0.785	0.648	0.990
ι	0.987	0.902	0.929	0.877
ψ	0.116	0.499	0.409	0.749
$R_{EQ,P}/R_{EQ,3D}$	1.266	1.017	0.936	-
η_P	0.239	0.740	0.603	-
$R_{EQ,O}/R_{EQ,3D}$	1.165	0.773	0.751	-
η_O	0.260	0.974	0.752	-

Table 5: Morphological parameters of the extracted droplet, see figure 24, of the HIT-like flow database.

718 **B.4 Droplet D)**



720 Figure 25: Distorted droplet extracted from the HIT-like flow database.

	2D			3D
	X	Y	Z	-
$R_{EQ,3D}/a$	0.731	0.776	0.822	0.717
$b/R_{EQ,3D}$	0.546	1.132	0.721	0.491
$R_{EQ}/R_{EQ,3D}$	0.917	1.215	0.960	-
α	0.400	0.878	0.592	0.352
η	0.860	0.130	0.517	0.904
ι	0.893	0.994	0.952	0.877
ψ	0.406	0.066	0.314	0.529
$R_{EQ,P}/R_{EQ,3D}$	1.007	1.234	1.022	-
η_P	0.815	0.128	0.486	-
$R_{EQ,O}/R_{EQ,3D}$	0.742	1.182	0.859	-
η_O	1.107	0.133	0.578	-

721 Table 6: Morphological parameters of the extracted droplet, see figure 25, of the HIT-like flow database.

721 **References**

722 [Adrian, 1991] Adrian, R. J. (1991). Particle-imaging techniques for experimental fluid mechanics. *Annual*
723 *review of fluid mechanics*, 23(1):261–304.

724 [Adrian, 2005] Adrian, R. J. (2005). Twenty years of particle image velocimetry. *Experiments in fluids*,
725 39(2):159–169.

726 [Bachalo and Houser, 1984] Bachalo, W. and Houser, M. (1984). Phase/doppler spray analyzer for simultane-
727 ous measurements of drop size and velocity distributions. *Optical Engineering*, 23(5):235583.

728 [Baert et al., 1992] Baert, L., Fanara, D., Remon, J. P., and Massart, D. (1992). Correlation of extrusion forces,
729 raw materials and sphere characteristics. *Journal of pharmacy and pharmacology*, 44(8):676–678.

730 [Belhadef et al., 2012] Belhadef, A., Vallet, A., Amielh, M., and Anselmet, F. (2012). Pressure-swirl atom-
731 ization: Modeling and experimental approaches. *International Journal of Multiphase Flow*, 39:13–20.

732 [Blaisot and Yon, 2005] Blaisot, J. and Yon, J. (2005). Droplet size and morphology characterization for dense
733 sprays by image processing: application to the diesel spray. *Experiments in fluids*, 39(6):977–994.

734 [Blott and Pye, 2008] Blott, S. J. and Pye, K. (2008). Particle shape: a review and new methods of characteri-
735 zation and classification. *Sedimentology*, 55(1):31–63.

736 [Bothell et al., 2020] Bothell, J. K., Machicoane, N., Li, D., Morgan, T. B., Aliseda, A., Kastengren, A. L.,
737 and Heindel, T. J. (2020). Comparison of x-ray and optical measurements in the near-field of an optically
738 dense coaxial air-assisted atomizer. *International Journal of Multiphase Flow*, 125:103219.

739 [Chan et al., 2021] Chan, W. H. R., Dodd, M. S., Johnson, P. L., and Moin, P. (2021). Identifying and tracking
740 bubbles and drops in simulations: A toolbox for obtaining sizes, lineages, and breakup and coalescence
741 statistics. *Journal of Computational Physics*, 432:110156.

- 742 [Charpentier et al., 2020] Charpentier, J.-B., Brändle de Motta, J., and Ménard, T. (2020). Capillary phe-
743 nomena in assemblies of parallel cylindrical fibers: From statics to dynamics. *International Journal of*
744 *Multiphase Flow*, 129:103304.
- 745 [Chen et al., 2019] Chen, T., Chéron, V., Guo, Z., Brändle De Motta, J. C., Ménard, T., and Wang, L.-P.
746 (2019). Simulation of immiscible two-phase flows based on a kinetic diffuse interface approach. *10th Int.*
747 *Conf. Multiph. Flow*, (2019).
- 748 [Chéron et al., 2019] Chéron, V., Brändle de Motta, J. C., Vaudor, G., Ménard, T., and Berlemont, A. (2019).
749 From droplets to particles: Transformation criteria. In *29th European Conference on Liquid Atomization*
750 *and Spray Systems*, page 8.
- 751 [Clift et al., 1978] Clift, R., Grace, J. R., and Weber, M. (1978). *Bubbles, Drops and Particles*. Academic
752 Press, New York.
- 753 [Cordesse et al., 2020] Cordesse, P., Remigi, A., Duret, B., Murrone, A., Ménard, T., Demoulin, F.-X., and
754 Massot, M. (2020). Validation strategy of reduced-order two-fluid flow models based on a hierarchy of
755 direct numerical simulations. *Flow, Turbulence and Combustion*, 105(4):1381–1411.
- 756 [Dodd and Ferrante, 2016] Dodd, M. S. and Ferrante, A. (2016). On the interaction of taylor length scale size
757 droplets and isotropic turbulence. *Journal of Fluid Mechanics*, 806:356–412.
- 758 [Dumouchel and Blaisot, 2013] Dumouchel, C. and Blaisot, J.-B. (2013). Multi-Scale Analysis of Liquid
759 Atomization Processes and Sprays. In *25th European Conference on Liquid Atomization and Spray Systems*,
760 Chania, Greece.
- 761 [Dumouchel and Blaisot, 2014] Dumouchel, C. and Blaisot, J.-B. (2014). Laser diffraction measurement of
762 nonspherical drop sprays. *Atomization and Sprays*, 24(3):223–249.
- 763 [Dumouchel et al., 2015] Dumouchel, C., Blaisot, J.-B., Bouche, E., Ménard, T., and Vu, T.-T. (2015). Multi-
764 scale analysis of atomizing liquid ligaments. *International Journal of Multiphase Flow*, 73:251–263.
- 765 [Duret et al., 2012] Duret, B., Luret, G., Reveillon, J., Ménard, T., Berlemont, A., and Demoulin, F.-X. (2012).
766 Dns analysis of turbulent mixing in two-phase flows. *International Journal of Multiphase Flow*, 40:93–105.
- 767 [Eriksson et al., 1997] Eriksson, M., Alderborn, G., Nyström, C., Podczec, F., and Newton, J. (1997). Com-
768 parison between and evaluation of some methods for the assessment of the sphericity of pellets. *Interna-*
769 *tional journal of pharmaceutics*, 148(2):149–154.
- 770 [Fdida and Blaisot, 2008] Fdida, N. and Blaisot, J. (2008). Morphological characterization of droplets. appli-
771 cation to atomization of sprays. *Proceedings of ISFV*, 13.
- 772 [Fdida et al., 2010] Fdida, N., Blaisot, J.-B., Floch, A., and Dechaume, D. (2010). Drop-size measurement
773 techniques applied to gasoline sprays. *Atomization and Sprays*, 20(2).
- 774 [Fedkiw et al., 1999] Fedkiw, R. P., Aslam, T., Merriman, B., Osher, S., et al. (1999). A non-oscillatory
775 eulerian approach to interfaces in multimaterial flows (the ghost fluid method). *Journal of Computational*
776 *Physics*, 152(2):457–492.
- 777 [Ficuciello et al., 2017] Ficuciello, A., Blaisot, J., Richard, C., and Baillot, F. (2017). Investigation of air-
778 assisted sprays submitted to high frequency transverse acoustic fields: Droplet clustering. *Physics of Fluids*,
779 29(6):067103.

- 780 [Ghaemi et al., 2008] Ghaemi, S., Rahimi, P., and Nobes, D. (2008). Measurement of droplet centricity and
781 velocity in the spray field of an effervescent atomizer. In *Int Symp on Applications of Laser Techniques to*
782 *Fluid Mechanics, Lisbon, Portugal*, pages 07–10. Citeseer.
- 783 [Ghaemi et al., 2009] Ghaemi, S., Rahimi, P., and Nobes, D. S. (2009). Assessment of parameters for distin-
784 guishing droplet shape in a spray field using image-based techniques. *Atomization and Sprays*, 19(9).
- 785 [González and García, 2009] González, H. and García, F. (2009). The measurement of growth rates in capil-
786 lary jets. *Journal of Fluid Mechanics*, 619:179.
- 787 [Green, 1975] Green, A. (1975). An approximation for the shapes of large raindrops. *Journal of Applied*
788 *Meteorology*, 14(8):1578–1583.
- 789 [Herrmann, 2010a] Herrmann, M. (2010a). Detailed numerical simulations of the primary atomization of a
790 turbulent liquid jet in crossflow. *Journal of Engineering for Gas Turbines and Power*, 132(6).
- 791 [Herrmann, 2010b] Herrmann, M. (2010b). A parallel eulerian interface tracking/lagrangian point particle
792 multi-scale coupling procedure. *Journal of Computational Physics*, 229(3):745–759.
- 793 [Kashdan et al., 2007] Kashdan, J. T., Shrimpton, J. S., and Whybrew, A. (2007). A digital image analy-
794 sis technique for quantitative characterisation of high-speed sprays. *Optics and Lasers in Engineering*,
795 45(1):106–115.
- 796 [Lamb, 1881] Lamb, H. (1881). On the vibrations of an elastic sphere. *Proceedings of the London Mathemat-*
797 *ical Society*, s1-13(1):189–212.
- 798 [Lebas et al., 2009] Lebas, R., Menard, T., Beau, P.-A., Berlemont, A., and Demoulin, F.-X. (2009). Numer-
799 ical simulation of primary break-up and atomization: Dns and modelling study. *International Journal of*
800 *Multiphase Flow*, 35(3):247–260.
- 801 [Malot and Blaisot, 2000] Malot, H. and Blaisot, J.-B. (2000). Droplet size distribution and sphericity mea-
802 surements of low-density sprays through image analysis. *Particle & Particle Systems Characterization:*
803 *Measurement and Description of Particle Properties and Behavior in Powders and Other Disperse Systems*,
804 17(4):146–158.
- 805 [Masuk et al., 2019] Masuk, A. U. M., Salibindla, A., and Ni, R. (2019). A robust virtual-camera 3d shape
806 reconstruction of deforming bubbles/droplets with additional physical constraints. *International Journal of*
807 *Multiphase Flow*, 120:103088.
- 808 [Mayor et al., 2005] Mayor, L., Silva, M., and Sereno, A. (2005). Microstructural changes during drying of
809 apple slices. *Drying technology*, 23(9-11):2261–2276.
- 810 [Ménard et al., 2007] Ménard, T., Tanguy, S., and Berlemont, A. (2007). Coupling level set/vof/ghost fluid
811 methods: Validation and application to 3d simulation of the primary break-up of a liquid jet. *International*
812 *Journal of Multiphase Flow*, 33(5):510–524.
- 813 [Moallemi et al., 2016] Moallemi, N., Li, R., and Mehravaran, K. (2016). Breakup of capillary jets with
814 different disturbances. *Physics of Fluids*, 28(1):012101.
- 815 [Mukherjee et al., 2019] Mukherjee, S., Safdari, A., Shardt, O., Kenjereš, S., and Van den Akker, H. E. A.
816 (2019). Droplet–turbulence interactions and quasi-equilibrium dynamics in turbulent emulsions. *Journal of*
817 *Fluid Mechanics*, 878.
- 818 [Peano, 1887] Peano, G. (1887). *Applicazioni geometriche del calcolo infinitesimale*. Fratelli Bocca.

- 819 [Perlekar et al., 2012] Perlekar, P., Biferale, L., Sbragaglia, M., Srivastava, S., and Toschi, F. (2012). Droplet
820 size distribution in homogeneous isotropic turbulence. *Physics of Fluids*, 24(6):065101.
- 821 [Podczeck et al., 1999] Podczeck, F., Rahman, S., and Newton, J. (1999). Evaluation of a standardised
822 procedure to assess the shape of pellets using image analysis. *International journal of pharmaceutics*,
823 192(2):123–138.
- 824 [Ravelet et al., 2011] Ravelet, F., Colin, C., and Risso, F. (2011). On the dynamics and breakup of a bubble
825 rising in a turbulent flow. *Physics of Fluids*, 23(10):103301.
- 826 [Rorato et al., 2019] Rorato, R., Arroyo, M., Andò, E., and Gens, A. (2019). Sphericity measures of sand
827 grains. *Engineering Geology*, 254:43 – 53.
- 828 [Rosales and Meneveau, 2005] Rosales, C. and Meneveau, C. (2005). Linear forcing in numerical simulations
829 of isotropic turbulence: Physical space implementations and convergence properties. *Physics of fluids*,
830 17(9):095106.
- 831 [Schober et al., 2002] Schober, P., Meier, R., Schäfer, O., and Wittig, S. (2002). Visualization and phase
832 doppler particle analysis measurements of oscillating spray propagation of an airblast atomizer under typical
833 engine conditions. *Annals of the New York Academy of Sciences*, 972(1):277–284.
- 834 [Sussman et al., 1998] Sussman, M., Fatemi, E., Smereka, P., and Osher, S. (1998). An improved level set
835 method for incompressible two-phase flows. *Computers & Fluids*, 27(5-6):663–680.
- 836 [Tanguy and Berlemont, 2005] Tanguy, S. and Berlemont, A. (2005). Application of a level set method for
837 simulation of droplet collisions. *International Journal of Multiphase Flow*, 31(9):1015–1035.
- 838 [Trontin et al., 2010] Trontin, P., Vincent, S., Estivalezes, J. L., and Caltagirone, J. P. (2010). Direct numerical
839 simulation of a freely decaying turbulent interfacial flow. *International Journal of Multiphase Flow*, 36(11-
840 12):891–907.
- 841 [van Beeck and Riethmuller, 1996] van Beeck, J. and Riethmuller, M. (1996). Rainbow phenomena applied
842 to the measurement of droplet size and velocity and to the detection of nonsphericity. *Applied optics*,
843 35(13):2259–2266.
- 844 [Vaudor et al., 2017] Vaudor, G., Ménard, T., Aniszewski, W., Doring, M., and Berlemont, A. (2017). A
845 consistent mass and momentum flux computation method for two phase flows. application to atomization
846 process. *Computers & Fluids*, 152:204–216.